



Southern African summer-rainfall variability, and its teleconnections, on interannual to interdecadal timescales in CMIP5 models.

Bastien Dieppois, Benjamin Pohl, Julien Crétat, Jonathan Eden, Moussa Sidibe, Mark New, Mathieu Rouault, Damian Lawler

► To cite this version:

Bastien Dieppois, Benjamin Pohl, Julien Crétat, Jonathan Eden, Moussa Sidibe, et al.. Southern African summer-rainfall variability, and its teleconnections, on interannual to interdecadal timescales in CMIP5 models.. *Climate Dynamics*, 2019, 53 (5-6), pp.3505-3527. 10.1007/s00382-019-04720-5 . hal-02281266

HAL Id: hal-02281266

<https://hal.science/hal-02281266>

Submitted on 4 Dec 2023

HAL is a multi-disciplinary open access archive for the deposit and dissemination of scientific research documents, whether they are published or not. The documents may come from teaching and research institutions in France or abroad, or from public or private research centers.

L'archive ouverte pluridisciplinaire **HAL**, est destinée au dépôt et à la diffusion de documents scientifiques de niveau recherche, publiés ou non, émanant des établissements d'enseignement et de recherche français ou étrangers, des laboratoires publics ou privés.

Southern African summer-rainfall variability, and its teleconnections, on interannual to interdecadal timescales in CMIP5 models

Dieppois, B, Pohl, B, Cretat, J, Eden, JM, Sidibe, M, New, M, Rouault, M & Lawler, D

Author post-print (accepted) deposited by Coventry University's Repository

Original citation & hyperlink:

Dieppois, B, Pohl, B, Cretat, J, Eden, JM, Sidibe, M, New, M, Rouault, M & Lawler, D 2019, 'Southern African summer-rainfall variability, and its teleconnections, on interannual to interdecadal timescales in CMIP5 models' *Climate Dynamics*, vol. 53, no. 5–6, pp. 3505–3527. <https://dx.doi.org/10.1007/s00382-019-04720-5>

DOI 10.1007/s00382-019-04720-5

ISSN 0930-7575

ESSN 1432-0894

Publisher: Springer

The final publication is available at Springer via <http://dx.doi.org/10.1007/s00382-019-04720-5>

Copyright © and Moral Rights are retained by the author(s) and/ or other copyright owners. A copy can be downloaded for personal non-commercial research or study, without prior permission or charge. This item cannot be reproduced or quoted extensively from without first obtaining permission in writing from the copyright holder(s). The content must not be changed in any way or sold commercially in any format or medium without the formal permission of the copyright holders.

This document is the author's post-print version, incorporating any revisions agreed during the peer-review process. Some differences between the published version and this version may remain and you are advised to consult the published version if you wish to cite from it.

Southern African summer-rainfall variability, and its teleconnections, on interannual to interdecadal timescales in CMIP5 models

Bastien Dieppois ^{1, 2, 3}, Benjamin Pohl ⁴, Julien Crétat ^{4, 5}, Jonathan Eden ¹, Moussa Sidibe ¹, Mark New ⁶, Mathieu Rouault ^{2, 7}, Damian Lawler¹

¹ Centre for Agroecology, Water and Resilience, Coventry University, Coventry, UK

² Department of Oceanography, MARE Institute, University of Cape Town, Cape Town, RSA

³ School of Geography, Earth and Environmental Sciences, University of Birmingham, Birmingham, UK

⁴ Centre de Recherches de Climatologie, UMR 6282 Biogéosciences, CNRS/Université de Bourgogne Franche Comté, Dijon, France

⁵ IPSL/Laboratoire des Sciences du Climat et de l'Environnement, CEA-CNRS-UVSQ, Université Paris Saclay, Gif-sur-Yvette, France

⁶ African Climate & Development Initiative, University of Cape Town, Cape Town, RSA

⁷ Nansen-Tutu Center for Marine Environmental Research, University of Cape Town, Cape Town, RSA

Correspondence to: Bastien Dieppois, Centre for Agroecology, Water and Resilience (CAWR), Coventry University, Ryton Gardens, Ryton on Dunsmore, Coventry, CV8 3LG, UK. E-mail: bastien.dieppois@coventry.ac.uk

Abstract This study provides the first assessment of CMIP5 model performances in simulating southern Africa (SA) rainfall variability in austral summer (Nov–Feb), and its teleconnections with large-scale climate variability at different timescales. Observed SA rainfall varies at three major timescales: interannual (2–8 years), quasi-decadal (8–13 years; QDV) and interdecadal (15–28 years; IDV). These rainfall fluctuations are, respectively, associated with El Niño Southern Oscillation (ENSO), the Interdecadal Pacific Oscillation (IPO) and the Pacific Decadal Oscillation (PDO), interacting with climate anomalies in the South Atlantic and South Indian Ocean. CMIP5 models produce their own variability, but perform better in simulating interannual rainfall variability, while QDV and IDV are largely underestimated. These limitations can be partly explained by spatial shifts in core regions of SA rainfall variability in the models. Most models reproduce the impact of La Niña on rainfall at the interannual scale in SA, in spite of limitations in the representation of ENSO. Realistic links between negative IPO are found in some models at the QDV scale, but very poor performances are found at the IDV scale. Strong limitations, *i.e.* loss or reversal of these teleconnections, are also noted in some simulations. Such model errors, however, do not systematically impact the skill of simulated rainfall variability. This is because biased SST variability in the South Atlantic and South Indian Oceans strongly impact model skills by modulating the impact of Pacific modes of variability. Using probabilistic multi-scale clustering, model uncertainties in SST variability are primarily driven by differences from one model to another, or comparable models (sharing similar physics), at the global scale. At the regional scale, *i.e.* SA rainfall variability and associated teleconnections, while differences in model physics remain a large source of uncertainty, the contribution of internal climate variability is increasing. This is particularly true at the QDV and IDV scales, where the individual simulations from the same model tend to differentiate, and the sampling error increase.

Keywords Southern African rainfall variability · Interannual to interdecadal timescales · Sea-surface temperature anomalies · Teleconnections · CMIP5 models

1. Introduction

Southern Africa (SA, south of 20°S) is known to be particularly vulnerable to climate change due to a combination of a naturally high degree of climate variability and high reliance on climate-sensitive activities, such as rain-fed agriculture (Conway et al. 2015). In particular, during the main rainy season, *i.e.* austral summer (Nov–Feb, NDJF), SA rainfall has been shown to vary over ranges of timescales from synoptic (3–7 days; *e.g.* Todd and Washington 1999; Hart et al. 2012; Macron et al. 2014) to decadal (≥ 10 years; *e.g.* Dyer and Tyson 1977; Tyson 1981 1986; Mason and Jury 1997, Dieppois et al. 2016), as well as potential complex interactions across timescales. For instance, Cook (2001) and Ratnam et al. (2014) proposed that El Niño Southern Oscillation (ENSO) generates atmospheric Rossby waves in the Southern Hemisphere, which could be responsible for longitudinal shifts of the South Indian Convergence Zone (SICZ), where synoptic-scale rain bearing systems that affect southern Africa, such as tropical-temperate troughs (TTTs), preferentially develop (Todd and Washington 1999; Hart et al. 2012; Macron et al. 2014). Similarly, Dieppois et al. (2016) and Pohl et al. (2018), highlighted that part of the non-linearity in the relationship between ENSO and summer SA rainfall, which is prominent at the interannual timescale, could be explained by interactions with the Interdecadal Pacific Oscillation (IPO) and the Pacific Decadal Oscillation (PDO) at the quasi-decadal (8–13 years; QDV) and interdecadal (15–28 years; IDV) timescales, respectively. These studies also suggested that ENSO-like shifts and modulations of the Walker circulation in response to the IPO and PDO are interacting with regional ocean-atmospheric circulations, such as the South Indian Ocean Dipole (Morioka et al. 2015), leading

to shifts in the SICZ and modulations of the TTT occurrence. However, despite the importance of these decadal timescales in SA rainfall variability, and their impact on societies, little has been done to examine the ability of global climate models, particularly those that constitute the Coupled Model Intercomparison Project-phase 5 (CMIP5), to reproduce such processes on interannual to interdecadal timescales.

Model-based studies in southern Africa have highlighted large differences between climate models, especially in their estimates of historical rainfall (Hewitson and Crane 2006; Nikulin et al. 2012; Kalogomou et al. 2013; Dieppois et al. 2015; Munday and Washington 2016 2018). While models reproduce the annual cycle of rainfall reasonably well, there are large discrepancies in rainfall amount, and in particular in austral summer (*e.g.* Dieppois et al. 2015; Munday and Washington 2016 2018). As illustrated in Fig. 1a-b, most CMIP5 models significantly overestimate summer-rainfall, especially in areas of greater rainfall such as the north-eastern region of southern Africa (where more than 60% of models show an average wet bias of $34 \text{ mm.months}^{-1}$ or +41%). However, long-term SA rainfall variability has been poorly studied despite of the extensive use of CMIP5 models for climate impact assessment.

Some authors have proposed that part of such bias in SA rainfall could be explained by significant model-dependency on the strength of the Angola Low amongst CMIP5 models (Munday and Washington 2016; Lazenby et al. 2016), but underlying drivers of these model uncertainties remain unclear. Such uncertainties in CMIP5 models could also be explained through misrepresentations of the linkage between regional circulation and large-scale modes of climate variability. This is, for instance, the case for ENSO (Dieppois et al. 2015), which has major influences on SA rainfall variability (*e.g.* Ropelewski and Halpert 1987 1989; Lindesay 1988; Mason and Jury 1997; Rouault and Richard 2005; Kane 2009; Cr  tat et al. 2012; Ratnam

et al. 2014; Hoell et al. 2015; Dieppois et al. 2016). Dieppois et al. (2015) thus pointed out that anomalous westward extensions of ENSO patterns in the CMIP5 models were leading to wet biases in SA during El Niño events, as a response to anomalously continental locations of the SICZ. This is consistent with recent findings from James et al. (2018), who identify too many TTTs, and too much rainfall from TTTs in HadGEM3-GC2. Similarly, decadal ENSO-like patterns related to the IPO and PDO, and their interactions with atmospheric regional circulations, which also play an important role in SA rainfall variability (Dieppois et al. 2016; Malherbe et al. 2016; Pohl et al. 2018), could potentially contribute to CMIP5 model uncertainties over the region. Decadal rainfall anomalies have, for instance, been shown to explain a large part of the persistent drought in this region between the 1960s and 1990s (*e.g.* Richard et al. 2001; Rouault and Richard 2005; Dieppois et al. 2016; Malherbe et al. 2016; Pohl et al. 2018).

At the global scale, decadal rainfall variance has been shown to be largely underestimated in the CMIP3 and CMIP5 models (Ault et al. 2012). Decadal sea-surface temperature (SST) variability is often underestimated in the Pacific (Ault et al. 2013; Laepple and Huybers 2014; Henley et al. 2017; Power et al. 2017) and overestimated in the North Atlantic (Ba et al. 2014; Menary et al. 2015). This suggests that future climate projections could poorly represent decadal variability, and offer a limited view of prolonged drought and hydro-meteorological risks. Underlying drivers of such model uncertainties however remain unclear, especially at these timescales, and might be region-dependent (Hawkins and Sutton 2009; Deser et al. 2012). So far, no study has attempted to address these issues in SA. Using a time-space approach based on spectral analysis and a probabilistic clustering, this study then aims to: i) identify potential key sources of uncertainties in the CMIP5 models at different timescales; ii) discuss the respective contributions of different model physics and internal climate variability to the

CMIP5 model uncertainties at those timescales; iii) better understand processes driving SA rainfall variability, especially using CMIP5 multimodel ensemble.

This paper is organized as follows. In section 2, the datasets and methods are described. In section 3, we analyse the ability of CMIP5 models to simulate observed timescales of summer SA rainfall variability. In section 4, we assess model skill to simulate global SST variability at decadal timescales, and the teleconnections between SA rainfall and global SST. In section 5, we discuss the potential uncertainties related to the sample sizes (*i.e.* length and number of simulations per model), and the capability of each model, using longer-term model simulations. We then show in section 6 how four contrasting CMIP5 models represent atmospheric bridges linking the Pacific Ocean and SA. Finally, our main results are interpreted and discussed in section 7.

2. Data & Methods

2.1. Observations

The Climatic Research Unit (CRU) dataset is used to compare observed and simulated summer SA rainfall variability (Harris et al. 2014; Table 1). The summer-rain region, which is here defined as the region where the wettest months occur in NDJF, extends to all the north-eastern part of southern Africa (Fig. 1c). To optimally investigate summer-rainfall variability and its teleconnections, a summer-rainfall index (SRI) has been constructed by averaging the values over the summer region, as displayed in Fig. 1c. According to Dieppois et al. (2016), the quality of the SRI is quite stable throughout the 20th century, as a satisfactory number of rain gauges was always available over the region. In addition, very similar results were found using Global Precipitation Climatology Centre full data reanalysis version 7.0 (Schneider et al. 2014).

To examine the summer teleconnections with global SSTs, we used the extended reconstructed SST version 4 (ERSST.v4) of the National Climatic Data Centre (Huang et al. 2015; Table 1). Version 4 does not use satellite data, and is thus coherent over the whole time period. It is not affected by the cold SST bias induced by the use of satellite observations at the end of the 20th century (Reynolds et al. 2002). Uncertainty related to the choice of the observed SST datasets has been assessed in Dieppois et al. (2016), who compared the composite SST anomalies associated with SA rainfall from ERSST.v4 to those obtained using the HadISST1 (Rayner et al. 2003) and COBE SST2 (Hirahara et al. 2014) datasets: an agreement greater than 90% between datasets was found regardless the timescale, ensuring the reliability of our reference SST dataset.

As recommended in Zhang et al. (2013), the 20th Century Reanalysis version 2c (20CR.v2c; Compo et al. 2006 2011) is used as reference to discuss the representation of atmospheric bridges between the Pacific Ocean and SA (Table 1). Such atmospheric bridges are here depicted through velocity potential (ϕ) and stream function (ψ) composite anomalies in the lower and upper troposphere (850–600 and 400–150 hPa). The 20CR.v2c assimilates only surface pressure, and uses monthly SST and sea ice distributions as boundary conditions. Such a modelling and data assimilation strategy that remains constant over the entire time period allows spectral decompositions in analysing atmospheric circulation across different timescales with a reduced sensitivity to time-varying availability of observational datasets. The density of the observational network, *e.g.* amounts of assimilated data, as well as the quality of the SST field used as boundary conditions, remains nevertheless an intractable problem. This is likely to reduce the quality of the reanalyses, and the consistency between its different members, for the first decades of the period (Pohl et al. 2018). However, atmospheric composite anomalies associated with SA rainfall from all reanalysis members were consistent and significantly

correlated with the ensemble mean, suggestive of weak inter-member uncertainty (Dieppois et al. 2016).

2.2. CMIP5 model output

Performances have been assessed against observations using historical runs from 28 CMIP5 models (Table 1), which simulate climate variability from the mid-19th century to the early 21st centuries, and are driven by observed estimate of anthropogenic and natural forcings (Taylor et al. 2012). Initialization schemes are model dependent. Models from the same institutions or different institutions can share (successive) versions of the same atmospheric, oceanic, land surface and sea-ice components, and, therefore use very similar physics for simulating some parameterized processes of the climate system (Table 2). The spatial resolutions also change from one model to another (Table 1). The ocean grids were interpolated on orthogonal curvilinear grid in some models, making comparison difficult with regular grids, and have thus been remapped on a regular 2°×2° resolution grid using bilinear interpolation.

To assess the contribution of internal climate variability, all calculations have been performed on each individual member, giving a total of 95 simulations (Table 1). In addition, to test the uncertainties associated with the sample sizes (*i.e.* length and number of simulations per model), which might be limiting at decadal timescale, longer-term pre-industrial control (piControl) simulations have been used in Section 5 (Table 1).

Model-simulated SRI has been calculated by averaging summer-rainfall amounts spatially in each historical and piControl runs from the 28 CMIP5 models (Fig. 1c). The simulated summer-rainfall region matched well with that observed, although their spatial extension sensibly varies from one model to another (Fig. 1c).

2.3. Timescales of variability and associated teleconnections

In section 3, we first compare the significant timescales of observed SRI variability with those simulated in the 95 members from the 28 selected CMIP5 models using fast Fourier transform (FFT). Significance tests of the FFT spectrum assumes a red-noise background spectrum for the null hypothesis, which is tested by 10,000 Monte Carlo simulations of first-order autoregressive (AR[1]) processes (Ghil et al. 2002). We next compare the SRI variance according to the three dominant timescales identified in observations (*i.e.* interannual: 2–8 year; QDV: 8–13 year; IDV: 15–28 year; Dieppois et al. 2016) by submitting observed and simulated time series to FFT band-pass filtering. To reduce trend effects (Wu et al. 2007), the SRI indices are preliminary detrended using a locally weighted linear regression, with span equal to the length of the data. We then compute the centered ratio of standard deviation (*rSD*), here expressed as a percentage:

$$centered.rSD = 1 - \frac{sd(SRI[obs]^t)}{sd(SRI[sim]^t)} \times 100 \quad (1)$$

where *sd* refers to the standard deviations of the time series, and *t* indicates the corresponding timescales. Statistical significance of equality between observed and simulated variance is estimated using a two-sided Fisher’s *F* test at $p = 0.05$. The same procedure is then applied to each grid-point over the SA region, and to global SST in section 4.

In section 4, we also assess the ability of CMIP5 models to simulate teleconnection between SRI and global SSTs. After replicating the filtering procedure described above to SST datasets, composite analyses are performed to construct typical states of global SSTs associated with SA rainfall fluctuations. Two sets of SST anomalies are produced for each timescale, where the SRI exceeds ± 1 standard deviation (*i.e.* wet and dry anomalies); the resulting composites thus describe the difference in SST between wet and dry conditions over SA. Statistical significance

is estimated by testing the difference in mean between wet and dry SST anomalies using a two-sided Student's t test at $p = 0.05$. When time series are serially correlated, the degrees of freedom are adjusted by recalculating the “effective sample size” (N^{eff}). This is given by the following approximation (Yue and Wang 2004):

$$\frac{N}{N^{\text{eff}}} = 1 + \frac{2}{N(N-1)(N-2)} \sum_{i=1}^t (N-i-1)(N-i-2)ts(i) \quad (2)$$

where N is the number of observations in the sample, $ts(i)$ is the serial correlation between ranks of the observations for lag i , and t is the maximum time lag considered. This procedure has then been replicated for piControl simulations in section 5, and to examine the performance of the models to reproduce atmospheric bridges between the Pacific basin and SA in section 6. Note that, while the present study aims at identifying climate processes associated with different ranges of SA rainfall fluctuations, some non-linearity between SST anomalies associated with wet and dry years only emerge at the interannual timescale (Fig. A1).

2.4. Assessing and narrowing model uncertainties

In sections 3 and 4, model performance is systematically assessed through Taylor diagrams (Taylor et al. 2001). As mentioned in earlier studies (Hawkins and Sutton 2009; Deser et al. 2012), at the regional scale, model uncertainties are increasing at decadal timescales due an increasing contributions of internal climate variability, adding to problems in model physics. This enhances diversity in the CMIP5 simulations, as simulations of the same model are likely to drift from one another, making meaningless the use of simple statistics (*e.g.* model mean and spread). Similarly to previous studies (*e.g.* Jun et al. 2008; Knutti et al. 2010 2013), a clustering approach has therefore been used to quantify the similarities between all models, and between simulations of the same model without predefined assumption. The relative contributions of model physics and internal climate variability could thus be discussed by assessing the inter-simulation spread within the CMIP5 framework, while identifying recurrent patterns.

The similarities between the 95 simulated spatial patterns of SA rainfall variability, global SST variability and composite SST anomalies (*cf.* sections 2.3-4), have thus been quantified at each timescale using Ward’s agglomerative criteria applied to Euclidean distances (Ward 1963; Crétat et al. 2018). In addition, we used a multi-scale bootstrap approach, allowing for estimation of the probability of each cluster (Shimodaira 2002, 2004), to optimize the identification of recurrent and spatially coherent clusters within the multimodel ensemble (Fig. A2). To estimate approximately unbiased probability that a cluster appears in the replicate, 10,000 bootstrap resampling over 33 different spatial lengths of the data (2% to 180% of the spatial domain, *i.e.* 330,000 iterations) are used (Fig. A2). Randomly resampling the spatial domain with different sizes thus enables to reduce the uncertainty associated with the selected grid-resolution, and to balance the weight of different regions (*e.g.* Pacific vs. Atlantic). Only clusters showing $p \geq 0.90$ have been considered as robust (Fig. A2). Clusters have been named as #CL1[pr]- to n [pr]-int for rainfall variability at the interannual timescale, and as #CL1[pr] to n [pr]-QDV and IDV at the QDV and IDV timescales (abbreviation [sstvar] and [sstano] have been used for clusters of global SST variance and composite anomalies, respectively).

In addition, in section 5, we discussed the sampling uncertainties in simulating observed statistics using historical and the longer-term piControl runs. The capability to significantly simulate observed SRI variance and global SST teleconnections at the three different timescales has been calculated by replicating the procedure described in section 2.3 for every 113 year time-period through the course of historical and piControl runs. The Fisher F test of equal variance at $p = 0.05$ and Pearson’s spatial correlation have been used to quantify the capability to simulate rainfall variance and SST teleconnection, respectively.

3. Summer SA rainfall variability

3.1. SRI variability

The ability of CMIP5 models to simulate SRI variability (including its timescales and variance) is displayed in Fig. 2. Corroborating Dieppo et al. (2016), observed SRI exhibits three significant timescales of variability over the 20th century (Fig. 2a): interannual (2–8 years), QDV (8–13 years) and IDV (15–28 years). Simulated and observed FFT spectra strongly differ (Fig. 2a). There are also large differences between FFT spectra from different models, and between simulations from the same model (Fig. 2a), indicating that CMIP5 simulations tend to produce their own variability.

However, as illustrated in Fig. A3, most models, and almost all institutions, can produce significant variability within the interannual, QDV and IDV timescales, suggesting that differences in simulated FFT spectra mostly result from internal climate variability, different resolutions and physics. The ratios of standard deviation between CMIP5 models and observation have thus been calculated at the three different timescales (Fig. 2b). CMIP5 models, perform better in simulating SRI variability at the interannual timescale (-6% average bias) than at the QDV and IDV timescales (-15 and -37% average bias; Fig. 2b). At the interannual timescale, more than 50% of the simulations show similar variance to observations (Fig. 2b), while significant underestimations and overestimations are detected in 35 and 14% of model simulations, respectively (Fig. 2b). At the QDV and IDV timescales, only about 30 and 14% of the CMIP5 simulations, respectively, show significant variance close to observation (Fig. 2b). These simulations always correspond to models producing realistic rainfall variance at the interannual timescale (Fig. 2b), suggesting cross-linkages between timescales in the model errors. Biases in simulating SRI variance are indeed proportionally stronger from the interannual to IDV timescales, especially for model simulations

underestimating SRI interannual variability (box plots on Fig. 2b). 51 and 77% of model simulations thus significantly underestimate SRI QDV and IDV, respectively (Fig. 2b).

3.2. Core regions of summer SA rainfall variability

3.2.1. Observations

Observed interannual rainfall variability explains approximately 70% of the total variance on average over SA (Fig. 3a). As for the raw data, interannual rainfall variability is clearly more pronounced in the northern and eastern regions (Fig. 3a), where summer-rainfall amounts are greater (Fig. 1a). At the QDV and IDV scales, which both can express more than 10% of the total variance over SA, similar patterns of rainfall variability are identified (Fig. 3a). The QDV is more pronounced on the eastern coastal regions of South Africa, but does not contribute much to total rainfall variability northeast of the central plateau (SA highlands; Fig. 3a), while the IDV is more pronounced in this region (Fig. 3a). In addition, according to earlier studies (Tyson 1981 1986; Mason and Jury 1997; Dieppois et al. 2016; Malherbe et al. 2016), the QDV can explain up to 26% of the total rainfall variance over the southwestern regions (Fig. 3a).

3.2.2. Model performances

CMIP5 models show good skills in simulating spatial patterns of summer SA rainfall variability at the interannual timescale (Fig. 4a). Spatial correlations between CMIP5 simulations and observation often exceed 0.7 (up to ≥ 0.9), while the normalized mean bias is lower than 1 (Fig. 4a). Model skills remain moderately good at the QDV and IDV timescales ($0.5 \leq r \leq 0.85$), although these scores substantially drop in some simulations at the IDV scale (approaching 0; Fig. 4c). Although some models substantially overestimate spatial variability at each timescale, simulated patterns of rainfall variability are often close to the observed one, suggesting similar patterns than in observation (Fig 4a-c).

3.2.3. CMIP5 model diversity

Multi-scale bootstrapped clustering has been used to identify the recurrent and spatially coherent patterns in simulating summer SA rainfall variability within the CMIP5 multimodel ensemble. While 13 significant clusters are identified at the interannual scale, model diversity substantially increases at the QDV and IDV timescales with 28 and 21 significant clusters, respectively (Fig. 4d).

At the interannual timescale, clusters primarily refer to the different models and institutions (Fig. 4d). Different parameterizations of the LMDZ atmospheric model however lead to differentiations of the distinct versions of the IPSL model (Fig. 4d). Similarly, CMCC-CESM, which includes carbon cycle feedbacks, differs from other CMCC models (Fig. 4d). Models from different institutions sharing the same atmospheric model (or different versions; Table 2) also tend to be clustered together at the interannual timescale (*e.g.* ACCESS1-0 and MOHC, CMCC-CESM and MPI, or CESM1-BCG and CCSM4; Fig. 4d). In addition, some models from different institutions (*e.g.* ACCESS1-3, CSIRO-Mk3-6-0 and MIROC5), are also regrouped (Fig. 4d). Although the similarities between these models could not be explain here through similarities in model physics, all these models are found to overestimate interannual SRI variability (Fig. 2).

At the QDV and IDV scales, individual simulations from the same or comparable models, gradually differentiate, increasing cluster diversity (Fig. 4d). For instance, four significant clusters emerge from CNRM-CM5 at the QDV scale, and this is also the case for most models (Fig. 4d). ACCESS1-3, CSIRO-Mk3-6-0 and MIROC5, which all overestimate interannual SRI variability, still have some simulations clustered together at the QDV and IDV timescales (Fig.

4d). This differentiation between simulations of the same models suggests larger contributions of internal climate variability to model biases. The different clusters could also still partly discriminate different model physics. This is confirmed in Fig. A4, as correlations between simulations from the same models decrease from interannual to IDV timescales, but remain stronger than correlations between different models.

3.2.4. *Simulated spatial patterns of SA rainfall variability*

Such diversity of simulated SA rainfall variability at the three different timescales is illustrated in Fig. 5. For clarity, names of model simulations describing each clusters are provided in Fig. A5.

According to observation, CMIP5 models generally simulate greater variability in the NE than in the SW regions regardless of the timescale (Fig. 5). However, slight misrepresentations of core regions of SA rainfall variability help explaining biases detected in SRI variability at all timescales. CMIP5 simulations overestimating SRI variability (#CL1[pr]-int, #CL1-2[pr]-QDV, #CL1, 6[pr]-IDV; Fig. A5) show very realistic patterns, but overestimate rainfall fluctuations in the north-west of the summer-rain region (Fig. 5a-c). In NASA-GISS models (#CL13[pr]-int, #CL5[pr]-QDV, #CL12[pr]-IDV; Fig. A5), rainfall variability is strongest in the eastern coastal regions of SA at all timescales, hence large underestimations further inland (Fig. 5a). At the interannual and QDV scales, MPI models and CMCC models (#CL10[pr]-int and #CL25[pr]-QDV; Fig. A5) simulate too strong rainfall variability in the western region, and underestimate it further east (Fig. 5a). Interestingly, the best performing simulations of SRI variability (#CL2, 6, 7, 10[pr]-int, #CL21, 24[pr]-QDV; Fig. A5) also show significant biases in rainfall variability over SA (Fig. 5a).

In summary, although the NE-SW gradient in SA rainfall variability is generally well reproduced for all timescales, slight shifts in core regions of SA rainfall variability could explain part of the biases in simulating SRI variability. This leads to great model diversity, suggesting contrasted links with large-scale and/or regional circulation patterns in CMIP5.

4. Interannual to interdecadal global SST variability and teleconnections with SA rainfall

We examine here the ability of CMIP5 models to simulate global modes of SST variability at these timescales, and their teleconnections with SA rainfall.

4.1. Observations

In observations, ENSO is the dominant mode of global SST variability at the interannual timescale (Mann and Park 1994; Klein et al 1999; Ghil et al. 2002; Sarachick and Cane 2010; De Viron et al. 2013), hence significant fluctuations in the equatorial Pacific at $p = 0.05$ (Fig. 3b). Positive SRI anomalies are thus primarily related to La Niña events, which are associated with cooler tropical Indian Ocean SSTs (Fig. 3c). Observed interannual SRI variability is also related to the South-West Indian Ocean SST dipole (Reason 1998; Reason and Mulenga 1999; Reason 2001; Behera and Yamagata 2001; Washington and Preston 2006; Hoell et al. 2017, 2018), the South Atlantic SST dipole (Fauchereau et al. 2003; Hermes and Reason 2005; Vigaud et al. 2009), and SST fluctuations reminiscent of Benguela Niños/Niñas (Lubbecke et al. 2010; Rouault 2012; Reason and Smart 2015).

The pattern of SST variability at the QDV timescale is similar to that of ENSO (Tourre et al. 1999 2001 2005; Fig. 3b). Wet conditions in SA are once again related to cold anomalies in the east Pacific flanked by a horseshoe pattern of opposite sign, confirming the results by Dieppois

et al. (2016). This is consistent with the negative IPO pattern after the definition provided by Power *et al.* (1999), and revisited by Di Lorenzo et al. (2015). This negative IPO occurs concomitantly with cold anomalies in the tropical Indian Ocean (Fig. 3c), as highlighted in Allan et al. (2003). Dipole SST anomalies in the South Atlantic Ocean and the SW Indian Ocean have also been related to SA rainfall at this timescale, in response to shifts in the atmospheric circulation (Venegas et al. 1996 1997; Dieppois et al. 2016). Climate anomalies in the SW Indian Ocean were however clearer in Jury et al. (2014) and Morioka et al. (2015), using a shorter period and other datasets.

As shown in Tourre et al. (1999 2001 2005), SST variability is particularly pronounced in the North Pacific at the IDV timescale (Fig. 3b). At this timescale, Pacific SST anomalies associated with SRI fluctuations display a horseshoe pattern, which is reminiscent of the PDO (*e.g.* Mantua et al. 1997; Mantua and Hare 2002; Newman et al. 2016). SRI fluctuations have also been connected to SST anomalies in the South Atlantic and Indian Oceans at the interdecadal timescale (Dieppois et al. 2016; Pohl et al. 2018). We thus note cold anomalies in the tropical Indian and South Atlantic Oceans, and warm anomalies in the extra-tropics (Fig. 3c). These regional SST anomalies in the adjacent oceans could be associated with enhanced atmospheric circulation in the Southern Hemisphere (Venegas et al. 1996 1997; Dieppois et al. 2016), and to the Southern Annular Mode (SAM; Ciasto et al. 2011; Malherbe et al. 2014 2016).

4.2. Model performances

The performance of CMIP5 models for simulating spatial patterns of global SST variability at the three different timescales are summarized in Fig. 6a. Their respective skills in simulating global SST anomalies associated with SA rainfall variability are displayed in Fig. 6b. Model performances in simulating global SST variability are reasonably good at the interannual

timescale (spatial correlation comprised between 0.45 and 0.75 against observations). Correlations gradually decrease at the QDV ($0.3 < r < 0.7$) and IDV ($0.1 < r < 0.65$) scales (Fig. 6a-b). For the teleconnections between SA rainfall and global SST (Fig. 6b), most models show correlations greater than 0.4 at the interannual timescale. Correlations are weaker at the QDV scale ($-0.6 < r < 0.7$) and weaker still at the IDV scale ($-0.4 < r < 0.4$; Fig. 6a-b).

Global SST variability can be too strong in CMIP5 models regardless the timescale (Fig. 6a). However, some regions, such as the Arctic and the Southern Ocean, strongly suffer from large uncertainties in observation due to data scarcity (Hirahara 2014; Huang et al. 2016). More specifically for SA rainfall, the teleconnections with global SST show very contrasted skills at all timescales, suggesting large model diversity.

4.3. Model diversity

The number of significant clusters of global patterns of SST variability (14, 13 and 15 from the interannual to IDV) and of global SST anomalies associated with SA rainfall (22, 24, 19) is almost constant regardless the timescale (Fig. 6c). The clusters of global SST variability patterns mostly discriminate resembling models (sharing some components or parameterizations; Table 2), in spite of some exceptions (like the different versions of the IPSL model). The situation is far less clear for global SST–SA rainfall teleconnections, especially at the QDV and IDV scales, where intra-ensemble similarities are as much or more important than inter-model similarities (Fig. A6). At these timescales, all CMIP5 model ensembles produce different clusters of global SST-SA rainfall teleconnections, suggesting major contributions of internal climate variability. For instance, CSIRO-Mk3-6-0 simulations, which were converging at the interannual scale, drift into 6 and 5 different clusters at the QDV and IDV scales (Fig. 6c).

4.4. Simulated global SST variability, and teleconnections with SA rainfall

CMIP5 model diversity in simulating global patterns of SST variability and SST-SA rainfall teleconnection is illustrated in Figs. 7 and 8, respectively. For clarity, names of model simulations describing each clusters are provided in Fig. A5.

At the interannual timescale, ENSO patterns are extending too far west and too tightly confined to the equator (AchutaRao and Sperber 2006; Capotondi et al. 2006, Lin 2007; Guilyardi et al. 2009; Fig. 7a), which could substantially impact SA rainfall variability, as suggested in Dieppois et al. (2015). Most models link wet conditions in SA to La Niña SST anomalies in the Pacific, and to cold tropical Indian Ocean (#CL4, 6, 9, 10[sstano]-int; Figs. 8a, A5). However, simulated La Niña SST anomalies extend too far west (*e.g.* #CL4, 6, 9[sstano]-int), and/or are too confined to the equatorial latitudes (#C10, 14[sstano]-int; Fig. 8a). These models also simulate the teleconnections with SA rainfall in the South Atlantic and South Indian Oceans (Fig. 8a), but SST anomalies there are too strong, given the systematic overestimations of SST variability (Fig. 7a). This systematic overestimations of SST variability could be due to limitations in simulating wind-stress in the mid-latitude and subtropical regions, which has been reported too strong by as much as 55% in CMIP3 and CMIP5 (Lee et al. 2013). These biases in the adjacent oceans have major implication for SA rainfall variability. As illustrated in Figure 9, even though most simulations (~60%) reproduce the main teleconnection with ENSO at interannual scale, only half of them lead to realistic representation of SA rainfall variability. This is because ENSO-induced large-scale climate anomalies are almost always associated with biased regional climate anomalies over the South Atlantic and South (and Tropical) Indian Oceans (Fig. 9), which can substantially modulate their impact on the continent (Hoell et al. 2017).

In other models (*e.g.* #CL7[sstano]-int.; Fig. A5), SA rainfall variability is not significantly related to ENSO at the interannual scale (Fig. 8a). In these models, interannual SRI variability is primarily linked to the South Indian and South Atlantic Oceans (Fig. 8a), denoting changes in the regional atmospheric circulation, *i.e.* changes in wind-stress modifying sensible and latent heat fluxes (Fauchereau et al. 2003). Such regional changes in SSTs could also be associated with the SAM (Ciasto et al. 2011), whose the component driven by ENSO (including the impact on austral summer-rainfall) is not captured in most CMIP5 models (Lim et al. 2016). Interestingly, although those regional climate anomalies are systematically biased, they can lead to good representation of SA rainfall variability (Fig. 9), suggesting error compensations. Underestimations of ENSO anomalies in austral summer could however be at least partly explained by misrepresentations of the seasonality in ENSO variability in some models (Fig. A7). For instance, ENSO activity is peaking between March and August in IPSL models, and is slightly delayed in ACCESS1-3 (Fig. A7). This is not true for CCSM4 and CESM-BCG, which show realistic seasonal timing in ENSO activity, even though largely overestimated (Fig. A7). In some CCSM4 simulations (#CL8[sstano]-int; Fig. A5), wet conditions occur during El Niño events (Fig. 8a), *i.e.* a reversed-sign association compared to observations.

At the QDV timescale, tropical SST variability in the central Pacific is far too weak in most CMIP5 models (Fig. 7b), suggesting large underestimations of IPO variability. In addition, according to Henley et al. (2017), CMIP5 models locate IPO variability too far west (#CL1, 2, 4, 8 and 12[sstvar]-QDV; Figs. 7b, A5). Some models thus simulate negative IPO anomalies associated with cold anomalies in the tropical Indian Ocean (#CL1, 21, 24[sstano]-QDV; Figs. 8b, A5). A skilful representation of the IPO teleconnection is however rarely associated with a good representation of SA rainfall variability (Fig. 9). We also systematically found SST dipole

anomalies in both the South Atlantic and South Indian Oceans (Fig. 8b). Interestingly, although, these climate anomalies in the adjacent oceans are biased in most models, they can lead to good reproduction of SA rainfall variability (Fig. 9). This suggests error compensations at the QDV scale also. Some models simulate weak or even reversed relationships between SA rainfall and Pacific SSTs (Fig. 2b). For instance, in #CL11 [sstano]-QDV (Fig. A5), wet conditions are linked to positive IPO (Fig. 8b).

At the IDV timescale, the PDO variability is systematically confined to the North Pacific in most CMIP5 models (Fig. 7c), while it should extend further in the tropics in response to ENSO forcing (Schneider and Cornuelle 2005). Very few simulations, which are the best performing in simulating SRI variability at this timescale (Fig. 2b), link wet conditions over SA to negative PDO anomalies (#CL1-2[sstano]-IDV; Figs. 8c, 9, A5). These simulations also simulate cold (warm) SST anomalies in the tropical (extra-tropical) Indian and South Atlantic Oceans (Fig. 8c). However, the same simulations tend to link SA rainfall to decadal ENSO-like SST anomalies, reminiscent of negative IPO in the tropical Pacific Ocean (Fig. 8c). Indeed, many simulations overestimate IPO-like variability in the equatorial Pacific at the IDV scale (*e.g.* #CL1, 11[sstvar]-IDV; Figs. 7c, A5). Although this could highlight systematic biases in CMIP5 models (*e.g.* Fleming and Anchukaitis 2016), concomitance between IPO and PDO patterns might arise from internal climate variability. In-phase variability of these low-frequency modes is very rare, and has not been observed at this timescale over the instrumental period (Fig. 3b-c).

5. Sample size uncertainties and model capabilities

With an increasing contribution of internal climate variability, regional model evaluations could be influenced by the sample sizes (*i.e.* length and number of simulations per model). This is

particularly true at decadal timescales, where historical runs only capture ~14 and ~7 life cycles of QDV and IDV, hence limiting the chance to match the observed “realisation”. In this section, we thus discuss the capability of each model by quantifying the chance to reproduce SRI variance and its global SST teleconnections for every 113 year time-period through the course of all historical runs and using the longer-term piControl simulations (Fig. 10). The number of samples used to quantify the model capabilities is not constant, and should be used as an indicator of robustness (Fig. 10).

At the interannual timescale, half of the CMIP5 models show very good capability ($> 80\%$) to significantly simulate SRI variance equal to observation in historical and piControl runs (Fig. 10a). In addition, model capabilities are most of the time weaker in piControl runs than historical runs (Fig. 10a), suggesting that interannual SA rainfall variability is strongly modulated by internal climate variability in longer runs. The capability to simulate significant similar SRI variance between models and observation progressively decreases at the QDV and IDV timescales (Fig. 9a). At the QDV timescale, ~75 and ~90% of CMIP5 models show moderate to low capability in historical and piControl runs, respectively (Fig. 9a). At the IDV timescale, a third and half of the CMIP5 models show some capability using historical and piControl runs, respectively (Fig. 9a). At the QDV and IDV scales, model capabilities are also generally greater in piControl runs than in historical runs (Fig. 9). This suggests that, at these decadal timescales, better performance could be obtained in many models using longer runs (or large-ensembles, which also account better for internal climate variability).

More mixed results are identified when analysing simulated teleconnections between SRI and global SST anomalies. At the interannual timescale, 50% and 70% of CMIP5 models show moderate to good capability in historical and piControl runs, respectively (Fig. 9b). Better

performance could have thus been found at the interannual scale using longer runs (or large-ensembles). Similar results are found at the QDV timescales, even if very few models show good capabilities. Model capabilities are however insensitive to the sample sizes, and are always null, at the IDV timescale (Fig. 10b).

Interestingly, capabilities in simulating global SST-SA rainfall teleconnection are always weaker than in SRI variance, which are generally greater at all timescales (Fig. 9a-b). This suggest that misrepresentations of atmospheric bridges between the Pacific and SA, and its links to the regional circulation (cf. Sect. 4.4), remain even through the course of piControl runs, and are very little sensitive to internal climate variability. In this regard, GFDL-CM3 could be considered as a reference in simulating both summer SA rainfall and their teleconnections at the interannual timescale (Fig. 10a-b). Some models, such as CSIRO-Mk3-6-0 and, in particular, MPI-ESM-LR, provide good capabilities to portray consistent interannual to QDV fluctuations in both teleconnections and SRI variability (Fig. 10a-b).

6. Atmospheric bridges

6.1. Observed atmospheric anomalies associated with SRI variability

Observed atmospheric bridges between the Pacific and SA are examined through velocity potential and stream function composite anomalies in the lower and upper troposphere (Fig. 11).

At the interannual timescale, La Niña SST events (which favour wet conditions over SA; Fig. 3c), are associated with large-scale lower-layer convergence over the western Pacific, and divergence over the eastern Pacific, and reverse signals in the upper troposphere (Fig. 11). This denotes conditions favourable to large-scale ascending motion over the Maritime Continent and

subsiding motions in the eastern Pacific, which is consistent with a westward shift and intensification of the Walker circulation. According to Hoell et al. (2015), changes in vertical winds and convection over the western Pacific result in tropospheric diabatic heating, which in turn force a Gill-Matsuno response over the Indian Ocean basin and surrounding continents (Fig. 11). The Gill-Matsuno response is materialized in the lower troposphere by significant cyclonic circulation poleward and westward of the anomalous diabatic heating over the Maritime Continent, while anticyclonic circulation is detected in the upper layers (Fig. 11). In the Southern Hemisphere, this initiates a Rossby wave-train between the tropics and SA (Hoskins and Ambrizzi 1993; Cook 2001), thereby evidenced by an anticyclonic ridge (Fig. 11). This contributes to an enhancement of the South Atlantic High. Dieppois et al. (2016) argued that westerlies driven by the South Atlantic High then converge with easterlies from the Indian Ocean, leading to ascending motions and convection in SA (Fig. 11). This pattern also corresponds to a westward shift of the SICZ, favouring wet conditions in SA.

Similar mechanisms are identified at the QDV and IDV scales, where both negative IPO and PDO anomalies are associated with a westward shift and intensification of the Walker-type circulation, as well as a Gill-Matsuno response over the Indian Ocean basin (Fig. 11). However, at the QDV timescale, the resulting Rossby wave-train shows a quasi-meridional propagation, and acts to enhance the South Indian High (Fig. 11). This promotes easterly moisture flux from the Indian Ocean (Dieppois et al. 2016), and convergence with south-easterly fluxes from the Atlantic (Fig. 11), increasing rainfall over SA.

At the interdecadal timescale, atmospheric anomalies are much weaker, consistently with the lower contributions of IDV to SA rainfall variability (Pohl et al. 2018). There, the Rossby wave-train, evidenced by cyclonic circulation over subtropical SA, and anticyclonic circulation

further north (Fig. 11), modulates the regional circulation over SA. At the same time, significant changes in the meridional circulations take place in the Southern Hemisphere, discernible as alternating cyclonic and anticyclonic circulations in the extra-tropics (Fig. 11). Dieppo et al. (2016) argued that such anomalies could help to enhance both the South Atlantic and South Indian Highs, and potentially the SAM (Malherbe et al. 2016), which then favours convergence and ascending motions over SA (Fig. 11).

6.2. Atmospheric anomalies associated with SRI variability in CMIP5 models

Fig. 12 displays circulation composite anomalies in the lower troposphere as simulated by four CMIP5 models with contrasted performances according to section 5.

In some models, neither rainfall variability nor their SST teleconnections are adequately simulated (Fig. 10). In GISS-E2-R-CC, for instance, underestimations of La Niña SST anomalies at the interannual timescale lead to a weak response of the atmosphere. Significant, but far too weak, ascending motions are identified over the western Pacific, and subsidence occurs over the eastern Pacific (Fig. 12). This is consistent with a westward shift and intensification of the Walker circulation, but the associated Gill-Matsuno response over the Indian Ocean is far too weak (Fig. 12). At the QDV and IDV scales, none of these circulation anomalies are simulated (Fig. 12). This is due to major difficulties in simulating IPO and PDO variability in the equatorial Pacific (Figs. 8, 9). Large underestimations of ENSO variability, which is a common feature in NASA-GISS models (Fig. A7), leads to underestimate SRI variability.

In other models, rainfall variability at the interannual and QDV timescales is adequately reproduced, but as a response to different large-scale ocean-atmospheric processes (Fig. 10). In

IPSL-CM5B-LR, for instance, the relationship between SA rainfall and ENSO is reversed, and consists of an eastward shift in the Walker circulation. Southward shifts of the South Atlantic and South Indian Highs are also identified, as well as ascendance over the eastern coast of Africa, potentially associated with warm SST there (Fig. 12). This increases rainfall over SA. At the QDV and IDV scales, none of the observed circulation anomalies are simulated (Fig. 12), due to unrealistic IPO and PDO variability (Figs. 7-8). Rainfall QDV is therefore not directly influenced by the Pacific Ocean, but by anomalously strong cyclonic circulations in the subtropics.

GFDL-CM3 is the best performing model at the interannual timescale (Fig. 10). The westward shift and intensification of the Walker circulation, as well as the Gill-Matsuno response over the Indian Ocean are well simulated (Fig. 12). The intensity and the location of the South Atlantic High, and thus convergence and ascendance over SA (*i.e.* the SICZ activity), fluctuate from one simulation to another (Fig. 12). Similarly, contrasting performances are obtained over the Pacific Ocean at the QDV and IDV timescales (Fig. 12): negative IPO-like and PDO-like circulation anomalies are detected in one simulation only. At these timescales, rainfall variability is primarily driven by enhanced activity in the subtropical Highs in the Southern Hemisphere, in approximate agreement with observations (Fig. 12).

MPI models perform well at the interannual and QDV timescales (Fig. 10). In MPI-ESM-LR, the westward shift and intensification of the Walker circulation associated with wet conditions in SA is realistic in all simulations at both timescales (Fig. 12). However, at the interannual timescale, the Gill-Matsuno response over the Indian Ocean in response to diabatic heating anomalies over the western Pacific is not reproduced (Fig. 12): this may reflect Indian Ocean SSTs, which are too cold, but further work is needed here. In MPI models, interannual rainfall

variability is then not directly linked to the Pacific Ocean, but to regional changes in the South Atlantic and South Indian Highs (Fig. 11), which could be related to the SAM (Ciasto et al. 2011). At the QDV timescale, the Gill-Matsuno response is simulated too far west, and is reversed compared to observation (Figs. 11-12), consistently with too cold SSTs over the Maritime continent (Fig. 8). Interestingly, strong anomalous Gill-Matsuno responses (e.g. r1i1p1) lead to overestimate SA rainfall QDV, while weak anomalous Gill-Matsuno response (e.g. r3i1p1) lead to underestimations (Figs. 2, 12).

Taken together, the results of this section show that, while atmospheric bridges between the Pacific Ocean and SA are crucial at all timescales in the observations, only few CMIP5 models are able to reproduce it. In some models, simulated rainfall in SA is likely to be associated with error compensations and strongly biased large-scale mechanisms even in cases where regional-scale properties are realistically reproduced.

7. Discussion & Conclusion

This study is a first assessment of CMIP5 model performances in simulating SA rainfall variability and its teleconnections with large-scale modes of variability at different timescales. Historical runs from 28 models, and their associated piControl run ensembles, have been used to document the weight of sampling errors and internal climate variability.

Firstly, we examined the ability of CMIP5 models to simulate realistic summer SA rainfall variability, which exhibits three major timescales in observation (Dieppo et al. 2016): interannual (2–8 years), QDV (8–13 years) and IDV (15–28 years). CMIP5 models produce their own variability, but tend to perform better in simulating interannual timescales of SRI variability. Indeed, most models strongly underestimate rainfall variability at the QDV and IDV

scales, suggesting a limited view of prolonged drought and hydro-meteorological risks in CMIP5 models over SA. Highest skills in simulating SRI QDV and IDV are however obtained with best performing models at the interannual timescale, suggesting cross-linkages in model biases between timescales which could be used to improve the future generations of climate models. These limitations in simulating SRI variability are partly due to spatial shifts in the core regions of rainfall variability.

Secondly, CMIP5 model performances in portraying global SST variability at the three different timescales was assessed, as well as their teleconnections with SA rainfall. In observation, wet rainfall conditions over SA are associated with cold SSTs in the Pacific, mostly driven by ENSO, the IPO and the PDO, which interact with regional climate anomalies in the South Atlantic and South Indian Ocean (Dieppois et al. 2016; Pohl et al. 2018). Most models reproduce La Niña effects on rainfall at the interannual timescale, in spite of biases in the representation of ENSO (*e.g.* AchutaRao and Sperber 2006; Guilyardi et al. 2009). At the QDV timescale, some models succeed in reproducing the association between the IPO and SA rainfall, but IPO variability is systematically too weak, and extends too far west (Henley et al. 2017). Similarly at the IDV timescale, very few models reproduce negative PDO anomalies. Yet, good performances in simulating the large-scale teleconnections with the Pacific do not systematically lead to good representation of SA rainfall variability. This is because Pacific modes of variability are most of the time associated with biased regional climate anomalies in the adjacent oceans to SA, which, according to Hoell et al. (2017), can substantially modulate their impact on the continent.

Some CMIP5 simulations do not reproduce, or even significantly reverse, the average link between SA rainfall and Pacific SST variability at the interannual and QDV scales. Even though

701 this result suggests strong model limitations, such an unlikely configuration has already been
702 observed in rare occasions: during the exceptionally strong El Niño event of 1997/98, for
703 instance (Lyon and Mason 2007). In IPSL models and ACCESS1-3, such an unlikely
704 association between SA rainfall and El Niño anomalies could be due to errors in modelling the
705 seasonality of ENSO (Fig. A7). CMIP5 model limitations in fully-capturing the relationship
706 between the SAM and ENSO, and their combined impact on summer-rainfall in the Southern
707 Hemisphere, could also be crucial, as suggested in Lim et al. (2016). However, such errors do
708 not systematically impact the realism of simulated rainfall variability here. This is because of
709 error compensations, mostly resulting from substantial overestimation of SST variability in the
710 South Atlantic and South Indian Oceans, leading to appropriate simulations of SA rainfall
711 variability.

712
713 All together these results also highlight the potential importance of the South Atlantic and
714 Indian Ocean SSTs for SA rainfall, as suggested in earlier studies (Nicholson and Kim 1997;
715 Reason 1998 2001; Reason et al. 1999; Hoell et al. 2015, 2017, 2018; Morioka et al. 2015), and
716 in modulating the skills of CMIP5 models. They also emphasize the need for process-oriented
717 studies rather than merely descriptive work for model evaluation, since statistically coherent
718 regional variability can be obtained from biased large-scale teleconnections and mechanisms.
719 This issue is of crucial importance for operational seamless predictions and future climate
720 projections (*e.g.* Mason 1998; Landman and Beraki 2012; Beraki et al. 2014; Landman et al
721 2017).

722
723 Thirdly, the respective contributions of model errors and internal climate variability to overall
724 uncertainties have been disentangled using probabilistic multi-scale clustering. This new
725 methodology is strongly recommended for future model evaluation studies at regional and

decadal scales to assess and narrow the impact of internal climate variability. At the global scale, model uncertainties in SST variability are primarily driven by differences from one model to another. At the regional scale, *i.e.* SA rainfall variability and associated teleconnections, model uncertainties are also mainly related to differences in model physics at the interannual timescale. At the QDV and IDV scales, however, individual simulations from the same models, or comparable models, progressively differentiate, which, consistently with Keenlyside et al. (2008), suggests larger contributions of internal climate variability. Uncertainties related to the sample size (length and number of simulations) have also been assessed using piControl runs, and suggest that better performances could be obtained, at least on interannual and QDV scales, in many CMIP5 models using longer-runs. Better impact-assessment of future prolonged drought and hydro-meteorological risks over SA could therefore be obtained using large-ensemble (*e.g.* Kay et al. 2015).

Acknowledgements

ERSST.v4, 20CR.v2, GPCC.v7 and COBE SST2 data were provided by the NOAA/OAR/ESRL PSD, Boulder, Colorado, USA, from their website at <http://www.esrl.noaa.gov/psd/>. The CRU TS 3.24.1 rainfall field were available from the Centre for Environmental Data Archival (CEDA) at <http://catalogue.ceda.ac.uk/uuid/3f8944800cc48e1cbc29a5ee12d8542d>. The authors would like to thank Noel Keenlyside, Thomas Toniazzo and Yushi Morioka for their helpful discussions.

References

AchutaRao K, Sperber KR (2006) ENSO simulation of coupled ocean-atmosphere models: are the current models better? *Clim Dyn* 27:1–15

Allan RJ, Lindesay JA, Reason CJC (2003) Multidecadal variability in the climate system over the Indian Ocean region during the austral summer. *J Clim* 8:185–1873.

Ault TR, Cole JE, St. George S (2012) The amplitude of decadal to multidecadal variability in precipitation simulated by state-of-the-art climate models. *Geophys Res Lett* 39: L21705. doi: 10.29/2012GL053424..

Ault TR, Deser C, Newman M, Emile-Geay J (2013) Characterizing decadal to centennial variability in the equatorial Pacific during the last millennium. *Geophys Res Lett* 40:3450–3456.

Ba J, Keenlyside N, Latif M, Park W, Ding H, Lohmann K, Mignot J, Menary M, Ottera O, Wouters B, Salas y Melia D, Oka A, Belluci A, Volodin E (2014) A multi-model comparison for Atlantic multidecadal variability. *Clim Dyn* 9:2333-2348.

Beraki AF, DeWitt DG, Landman WA, Olivier C (2014) Dynamical Seasonal Climate Prediction Using an Ocean-Atmosphere Coupled Climate Model Developed in Partnership between South Africa and the IRI. *J Clim* 27:1719–1741.

Capotondi A, Wittenberg A, Masina S (2006) Spatial and temporal structure of Tropical Pacific interannual variability in 20th century coupled simulations. *Ocean Modelling* 15:274–278.

Ciasto LM, Alexander MA, Deser C, and England MH (2011) On the persistence of cold-season SST anomalies associated with the Annular Mode. *J Clim* 24:2500–2515.

Compo GP, Whitaker JS, and Sardeshmukh PD (2006) Feasibility of a 100 year reanalysis using only surface pressure data. *Bull Amer Met Soc* 87:175–190.

Compo GP, Whitaker JS, Sardeshmukh PD, Matsui N, Allan RJ, Yin X, Gleason BE, Vose RS, Rutledge G, Bessemoulin P, Brönniman S, Brunet M, Crouthamel RI, Grant AN., Groisman PY, Jones JD, Kruk M, Kruger AC, Marshall GJ, Maugeri M, Mok HY, Nordli Ø, Ross TF, Trigo RM, Wang XL, Woodruff SD, Worley SJ (2011) The twentieth century reanalysis project. *Quarterly J Roy Meteorol Soc* 137:1–28.

776 Conway D (2015) Climate and southern Africa's water-energy-food nexus. *Nat Clim Change*
 777 5:837–846.

778 Cook KH (2001) A Southern Hemisphere wave response to ENSO with implications for
 779 southern Africa precipitation. *J Atmos Sci* 15:2146–2162.

780 Crétat J, Pohl B, Dieppois B, Berthou S, Pergaud J (2018) The Angola Low: relationship with
 781 southern African rainfall and ENSO. *Climate Dynamics* Published online.
 782 doi.org/10.1007/s00382-018-4222-3

783 Crétat J, Richard Y, Pohl B, Rouault M, Reason CJC, Fauchereau N (2012) Recurrent daily
 784 rainfall patterns over South Africa and associated dynamics during the core of the austral
 785 summer. *Int J Climatol* 32:261–273.

786 De Viron O, Dickey JO, Ghil M (2013) Global modes of variability. *Geophys Res Let* 40:1832–
 787 1837.

788 Deser C, Phillips A, Bourdette V, Teng H (2012) Uncertainty in climate change projections:
 789 the role of internal climate variability. *Clim Dyn* 38:527–546.

790 Dieppois B, Rouault M, New M (2015) The impact of ENSO on Southern African rainfall in
 791 CMIP5 ocean atmosphere coupled climate models. *Clim Dyn* 45:2425–2442.

792 Dieppois B, Pohl B, Rouault M, New M, Lawler D, Keenlyside N (2016) Interannual to
 793 interdecadal variability of winter and summer southern African rainfall, and their
 794 teleconnections. *J Geophys Res-Atmos* 121: 6215–6239

795 Di Lorenzo E, Liguori G, Schneider N, Furtado JC, Anderson BT, Alexander MA (2015) ENSO
 796 and meridional models: A null hypothesis for Pacific climate variability. *Geophys Res Let*
 797 42:9440–9448.

798 Fauchereau N, Trzaska S, Richard Y, Roucou P, Camberlin P (2003) Sea-surface temperature
 799 co-variability in the southern Atlantic and Indian Oceans and its connections with the
 800 atmospheric circulation in the Southern Hemisphere. *Int J Clim* 23:663–677.

Fleming LE, Anchukaitis KJ (2016) North Pacific decadal variability in the CMIP5 last millennium simulations. *Clim Dyn* 47:3783–3801.

Ghil M, Allen MR, Dettinger MD, Ide K, Kondrashov D, Mann ME, Robertson AW, Saunders A, Tian Y, Varadi F, Yiou P (2002) Advanced spectral methods for climatic time series. *Reviews of Geophysics* 40:3-1-3-41.

Guilyardi E, Wittenberg A, Fedorov A, Collins M, Wang C, Capotondi A, van Oldenborg GJ, Stockdate T (2009) Understanding El Niño in Ocean-Atmosphere General Circulation Models: Progress and Challenges. *Bull Amer Meteor Soc* 90:325–340.

Harris I, Jones PD, Osborn TJ, Lister DH (2014) Updated high-resolution grids of monthly climatic observations - the CRU TS3.10 Dataset. *Int J Clim* 34:623–642.

Hart NCG, Reason CJC, Fauchereau N (2012) Cloud bands over southern Africa: seasonality, contribution to rainfall variability and modulation by the MJO. *Clim Dyn* 41:119–1212.

Hawkins E, Sutton R (2009) The potential to Narrow Uncertainty in Regional Climate Predictions. *Bull Amer Meteor Soc* 90:1095–1108.

Henley BJ, Meehl G, Power SB, Folland CK, King A, Brown JN, Karoly DJ, Delage F, Gallant AJE, Freund M, Neukom R (2017) Spatial and temporal agreement in climate model simulations of the Interdecadal Pacific Oscillation. *Environ Res Lett* 12:044011.

Hermes JC, Reason CJC (2005) Ocean Model Diagnosis of Interannual Coevolving SST Variability in the South Indian and South Atlantic Oceans. *J Clim* 18:2864–2882.

Hewitson BC, Crane RG (2006) Consensus between GCM climate change projections with empirical downscaling: precipitation downscaling over South Africa. *Int J Clim* 26:1315–1337.

Hiraha S, Ishii M, Fukuda Y (2014) Centennial-scale sea surface temperature analysis and its uncertainty. *J Clim* 27:57–75.

825 Hoell A, Funk C, Magadzire T, Zinke J, Husak G (2015) El Niño-Southern Oscillation diversity
826 and Southern Africa teleconnections during Austral Summer. *Clim Dyn* 45:1583–1599.

827 Hoell A, Funk C, Zinke J, Harrison L (2017) Modulation of the Southern Africa precipitation
828 response to the El Niño Southern Oscillation by the subtropical Indian Ocean Dipole. *Clim*
829 *Dyn* 48:2529–2540.

830 Hoell A, Cheng L (2018) Austral summer Southern Africa precipitation extremes forced by the
831 El Niño Southern Oscillation and the subtropical Indian Ocean Dipole. *Clim Dyn* 50:3219–
832 3236.

833 Hoskins BJ, Ambrizzi T (1993) Rossby Wave Propagation on a Realistic Longitudinally
834 Varying Flow. *J Atmos Sci* 50:1661–1671.

835 Huang B, Banzon VF, Freeman E, Lawrimore J, Liu W, Peterson TC, Smith TM, Thorne PW,
836 Woodruff SD, Zhang HM (2015) Extended Reconstructed Sea Surface Temperature Version
837 4 (ERSST.v4). Part I: Upgrades and Intercomparisons. *J Clim* 28:911–930.

838 Huang B, Thorne PW, Smith TM, Liu W, Lawrimore J, Banzon F, Zhang H-M, Peterson TC,
839 Menne M (2015) Further Exploring and Quantifying Uncertainties or Extended
840 Reconstructed Sea Surface Temperature (ERSST) Version 4 (v4). *J Clim* 29:3119–3142.

841 James R, Washington R, Abiodun B, Kay G, Mutemi J, Pokam W, Hart N, Artan G, Senior C
842 (2018) Evaluating climate models with an African lens. *Bull Amer Meteor Soc* 99:313–336.

843 Jun M, Knutti R, Nychka DW (2008) Local eigenvalue of CMIP3 climate model errors. *Tellus*
844 *A* 60:992–1000.

845 Kalogomou EA, Lennard C, Shongwe M, Pinto I, Favre A, Kent M, Hewitson B, Dosio A,
846 Nikulin G, Panitz H-J, Buchner M (2013) A Diagnostic Evaluation of Precipitation in
847 CORDEX Models over Southern Africa. *J Clim* 26:9477–9506.

848 Kane RP (2009) Periodicities, ENSO effects and trends of some South African rainfall series:
849 an update. *S Afr J Sci* 105:199–207.

Kay JE, Deser C, Phillips A, Mai A, Hannay C, Strand G, Arblaster JM, Bates SC, Danabasoglu G, Edwards J, Holland M, Kushner P, Lamarque J, Lawrence D, Lindsay K, Middleton A, Munoz E, Neale R, Oleson K, Polvani L, Vertenstein M (2015) The Community Earth System Model (CESM) Large Ensemble Project: A Community Resource for Studying Climate Change in the Presence of Internal Climate Variability. *Bull Amer Meteor Soc* 96: 1333–1349

Keenlyside NS, Latif M, Jungclauss J, Kornblueh L, Roeckner E (2008) Advancing decadal-scale climate prediction in the North Atlantic sector. *Nature* 453:84–88.

Klein SA, Soden BJ, Lau NC (1999) Remote sea surface variations during ENSO: evidence for a tropical atmospheric bridge. *J Clim* 12:917–932.

Knutti R. (2010) The end of model democracy? *Climatic Change* 102:395–404.

Knutti R, Meehl GA, Allen R, Stainforth DA (2006) Constraining climate sensitivity from the seasonal cycle in surface temperature. *J Clim* 19:4224–4233.

Laeppele T, Huybers P (2014) Ocean surface temperature variability: Large model-data differences at decadal and longer periods. *Proc Natl Acad Sci* 111:16682–16687.

Landman WA, Beraki A (2012) Multi-model forecast skill for mid-summer rainfall over southern Africa. *Int J Clim* 32:303–314.

Landman WA, Engelbrecht F, Hewitson B, Malherbe J, van der Merwe J (2017) Towards bridging the gap between climate change projections and maize producers in South Africa. *Theor Appl Climatol* 132:1153–1163.

Lazenby C, Todd M, Wang Y (2016) Climate model simulation of South Indian Ocean Convergence Zone: Mean state and variability. *Clim Res* 68:59–71.

Lee T, Waliser DE, Li JL, Landerer FW, Gierach MM (2013) Evaluation of CMIP3 and CMIP5 Wind Stress Climatology Unising Satellite Measurements and Atmospheric Reanalysis Produc. *J Clim* 26:5810–5826.

875 Lim E-P, Hendon HH, Arblastger JM, Delage F, Nguyen H, Min S-K, Wheeler MC (2016) The
876 impact of the Southern Annular Mode on Future changes in Southern Hemisphere rainfall.
877 *Geophys Res Lett* 43:7160–7167.

878 Lin J-L (2007) The Double ITCZ Problem in IPCC AR4 Couple GCMs: Ocean–Atmosphere
879 Feedback Analysis. *J Clim* 20:4497–4525.

880 Lindesay JA (1988) South African rainfall, the Southern Oscillation and a Southern Hemisphere
881 semi-annual cycle. *J Climatol* 8:17–30.

882 Lübbecke JF, Böning CW, Keenlyside NS, Xie S-P (2010) On the connection between
883 Benguela and equatorial Atlantic Niños and the role of the South Atlantic Anticyclone. *J*
884 *Geophys Res-Oceans* 115:C0915. doi:10.1029/2009JC005964.

885 Lyon B, Mason SJ (2007) The 1997-98 summer season in southern Africa. Part I: Observations.
886 *J Clim* 20:5134–5148.

887 Macron C, Pohl B, Richard Y, Bessafi M (2014) How do tropical-temperate troughs form and
888 develop over southern Africa? *J Clim* 27:1633–1647.

889 Malherbe J, Landman WA, Engelbrecht FA (2014) The bi-decadal rainfall cycle, Southern
890 Annular Mode and tropical cyclones over the Limpopo River Basin, southern Africa. *Clim*
891 *Dyn* 42:3121–3138.

892 Malherbe J, Dieppois B, Maluleke P, Van Staden M, Pillay DL(2016) South African droughts
893 and decadal variability. *Nat. Hazards* 80:657–681.

894 Mann ME, Park J (1994) Global modes of surface temperature variability on interannual to
895 century timescales. *J Geophys Res-Atmos* 99:25819–25833.

896 Mantua NJ, Hare SR (2002) The Pacific Decadal Oscillation. *J Oceanogr* 58:35–44.

897 Mantua NJ, Hare SR, Zhang Y, Wallace JM, Francis RC (1997), A Pacific Interdecadal Climate
898 Oscillation with Impacts on Salmon Production. *Bull Amer Meteor Soc* 78:1069–1079.

899 Mason SJ (1998) Seasonal forecasting of South Africa rainfall using a non-linear discriminant
900 analysis model. *Int J Clim* 18:147–164.

901 Mason SJ, Jury M (1997) Climatic variability and change over the Southern Africa: a reflection
902 on underlying processes. *Prog Phys Geo* 21:23–50.

903 Menary MB, Hodson DLR, Robson JI, Sutton RT, Wood RA, Hunt JA (2015) Exploring the
904 impact of CMIP5 model biases on the simulation of North Atlantic decadal variability.
905 *Geophys Res Lett* 42:5926–5934.

906 Morioka Y, Engelbrecht F, Behera S (2015) Potential sources of multidecadal climate
907 variability over southern Africa. *J Clim* 28:8695–8709.

908 Munday C, Washington R (2016) Circulation controls on southern African precipitation in
909 coupled models: The role of the Angola Low. *J Geophys Res-Atmos* 122:861–877.

910 Munday C, Washington R (2018) Systematic Climate Model Rainfall Biases over Southern
911 Africa: Links to Moisture Circulation and Topography. *J Clim* 31:7533–7548.

912 Newman M, Alexander MA, Ault T, Cobb KM, Deser C, Di Lorenzo E, Mantua NJ, Miller AJ,
913 Minobe S, Nakamura H, Schneider N, Vimont DJ, Phillips AS, Scott JD, Smith CA (2016)
914 The Pacific Decadal Oscillation, Revisited. *J Clim* 29:4399–4427.

915 Nicholson SE, Kim J (1997) The relationship of the El Niño-Southern Oscillation to African
916 rainfall. *Int J Clim* 17:117–135.

917 Nikulin G, Jones C, Giorgi F, Asrar G, Buchner M, Cerezo-Mota R, Christensen OB, Déqué
918 M, Fernandez J, Hansler A, van Meijgaard E, Samuelsson P, Sylla MB, Sushama L (2012)
919 Precipitation Climatology in an Ensemble of CORDEX-Africa Regional Climate
920 Simulations. *J Clim* 25:6057–6078.

921 Pohl B, Dieppois B, Crétat J, Lawler DM, Rouault M (2018) From synoptic to interdecadal
922 variability in southern African rainfall: towards a unified view across timescales. *J Clim*
923 31:5845–5872.

924 Power S, Casey T, Folland CK, Colman A, Mehta V (1999) Inter-decadal modulation of the
 925 impact of ENSO on Australia. *Clim Dyn* 15:319–323.

926 Power S, Delage F, Wang G, Smith I, Kociuba G (2017) Apparent limitations in the ability of
 927 CMIP5 climate models to simulate recent multi-decadal change in surface temperature:
 928 implications for global temperature projections. *Clim Dyn* 49:53–69.

929 Ratnam JV, Behera SK, Masumoto Y, Yamagata T (2014) Remote effects of El Niño and
 930 Modoki events on the Austral Summer Precipitation of Southern Africa. *J Clim* 27:3802–
 931 3815.

932 Rayner NA, Parker DE, Horton EB, Folland CK, Alexander LV, Rowell DP, Kent EC, Kaplan
 933 A (2003) Global analyses of sea surface temperature, sea ice, and night marine air
 934 temperature since the late nineteenth century. *J Geophys Res-Atmos* 108:4407.
 935 doi:10.1029/2002JD002670

936 Reason CJC (1998) Warm and cold events in the southeast Atlantic/southwest Indian Ocean
 937 region and potential impacts on circulation and rainfall over southern Africa. *Meteorog*
 938 *Atmos Phys* 69:49–65.

939 Reason CJC (2001) Subtropical Indian Ocean SST dipole events and southern African rainfall.
 940 *Geophys Res Lett* 28:2225–2227.

941 Reason CJC, Mulenga H (1999) Relationships between South African rainfall and SST
 942 anomalies in the southwest Indian Ocean. *Int J Climatol* 19:1651–1673.

943 Reason CJC, Smart S (2015) Tropical south east Atlantic warm events ad associated rainfall
 944 anomalies over southern Africa. *Front Environ Sci* 3:1-11. doi:10.3389/fenvs.2015.00024

945 Reynolds RW, Rayner NA, Smith TM, Stokes DC, Wang W (2002) An improved in situ and
 946 satellite SST analysis for climate. *J. Clim.*, **15**, 1609–1625.

947 Richard Y, Fauchereau N, Poccarrd I, Rouault M, Trzaska S (2001) XXth century droughts in
 948 Southern Africa: spatial and temporal variability, teleconnections with oceanic and
 949 atmospheric conditions. *Int. J. Clim.*, **21**, 873–885.

950 Ropelewski CF, Halpert MS (1987) Global and regional scale precipitation patterns associated
 951 with the El Niño/Southern Oscillation. *Mon Wea Rev* 115:1606–1626.

952 Ropelewski CF, Halpert MS (1989) Precipitation patterns associated with the high indices
 953 phase of the southern oscillation. *J Clim* 2:268–284.

954 Rouault M (2012) Bi-annual intrusion of tropical water in the northern Benguela upwelling.
 955 *Geophys Res Lett* 39:L12606. doi:10.1029/2012GL052099

956 Rouault M, Richard Y (2005) Intensity and spatial extent of droughts in Southern Africa.
 957 *Geophys Res Lett* 32:L15702. doi:10.1029/2005GL022436.

958 Sarachick ES, Cane MA (2010) *The El Niño-Southern Oscillation Phenomenon*. Cambridge
 959 University Press, Cambridge.

960 Schneider N, Cornuelle BD (2005) The forcing of the Pacific Decadal Oscillation. *J Clim*
 961 18:4355–4373.

962 Schneider U, Becker A, Finger P, Meyer-Christoffer A, Ziese M, Rudolf B (2014) GPCC's new
 963 land surface precipitation climatology based on quality controlled in situ data and its role in
 964 quantifying the global water cycle. *Theor Appl Climatol* 115:15–40.

965 Shimodaira H (2002) An approximately unbiased tests of phylogenetic tree selection.
 966 *Systematic Biology* 51:492–508.

967 Shimodaira H (2004) Approximately unbiased tests of regions using multistep-multiscale
 968 bootstrap resampling. *Annals of Statistics* 32:2616–2641.

969 Taylor KE, Stouffler RJ, Meehl GA (2012) An overview of CMIP5 and the experiment design.
 970 *Bull Am Meteorol Soc* 93:485–498.

971 Todd MC, Washington R (1999) Circulation anomalies associated with tropical-temperate
 972 troughs in southern Africa and the southwest Indian Ocean. *Clim Dyn* 15:937–951.

973 Tourre YM, Cibot C, Terray L, White WB, Dewitte B (2005) Quasi-decadal and inter-decadal
 974 climate fluctuations in the Pacific Ocean from a CGCM. *Geophys Res Lett* 32:L07710.
 975 doi:10.1029/2004GL022087

976 Tourre YM, Kushnir Y, White WB (1999) Evolution of interdecadal variability in sea level
 977 pressure, sea surface temperature, and upper ocean temperature over the Pacific Ocean. *J*
 978 *Phys Oceanogr* 9:1528–1541.

979 Tourre YM, Rajagopalan B, Kushnir Y, Barlow M, White WB (2001) Patterns of coherent
 980 ocean decadal and interdecadal climate signals in the Pacific basin during the 20th century.
 981 *Geophys Res Lett* 28:2069–2072.

982 Trenberth K (1997) The Definition of El Niño. *Bull Am Meteorol Soc* 78:2771–2778.

983 Tyson PD (1981) Atmospheric circulation variations and the occurrence of extended wet and
 984 dry spells over southern Africa. *J Climatol* 1:115–130.

985 Tyson PD (1986) *Climatic Change and variability over southern Africa*. Oxford University
 986 Press, Cape Town.

987 Venegas S, Mysak LA, Straub DN (1997) Atmosphere-ocean coupled variability in the South
 988 Atlantic. *J Clim* 10:2904–2920.

989 Vigaud N, Richard Y, Rouault M, Fauchereau N (2009) Moisture transport between the South
 990 Atlantic Ocean and southern Africa: relationships with summer rainfall and associated
 991 dynamics. *Clim Dyn* 32:113–123.

992 Ward JH (1963) Hierarchical Grouping to Optimize an Objective Function. *Journal of the*
 993 *American Statistical Association* 58:236–244.

994 Washington R, Preston A (2006) Extreme wet years over southern Africa: Role of Indian Ocean
 995 sea surface temperatures. *J Geophys Res-Atmos* 111:D15104. doi:10.1029/2005JD006724

996 Wu Z, Huang NE, Long SR, Peng C-K (2007) On the trend, detrending, and variability of
997 nonlinear and nonstationary time series. *Proc Natl Acad Sci USA* 104:14889–14894.

998 Yue S, Wang C (2004) The Mann-Kendall test modified by effective sample size to detect trend
999 in serially correlated hydrological series. *Water Resources Management* 18:201–218.

1000 Zhang Q, Kornich H, Holmgren K (2013) How well do reanalyses represent the southern
1001 African precipitation. *Clim Dyn* 40:951–962.

1002

1003

1004

1005

1006

1007

1008

1009

1010

1011

1012

1013

1014

1015

1016

1017

1018

1019

1020

Figures and Captions

Table 1 Summarized information on observation data and CMIP5 models used in the study.

Table 2 Different components of CMIP5 CGCMs used in the study. Shades of orange, blue, green and grey indicate shared components between CGCMs from different institutions.

Fig. 1 Summer (NDJF) differences between simulated and observed SA rainfall fields. **a** Multimodel mean of 95 historical runs from 28 CMIP5 models of summer-rainfall average minus the CRU TS 3.24.01 observations, compared to the NDJF rainfall climatology (*black dashed contours*), between 1901 and 2005. Statistical significance of differences in mean (*white colours*) has been estimated using a Student *t*-test at $p = 0.05$. **b** CMIP5 Multimodel agreement in the difference in summer-rainfall average compared with observation **c** Spatial distribution of the summer-rainfall region in the CMIP5 models (*coloured contours refer to each individual model; cf. Table 1*) and in the CRU TS 3.24.01 observations (*grey shaded*). **d** Multimodel agreement in the location of the summer-rainfall region in the CMIP5 models compared to observation (*grey contour*). The summer-rainfall region, which is used to calculate the SRI, has been defined as the area in which the wettest month of the year occur between November and February on average between 1901 (1850/60) and 2005 in the observations (CMIP5 models).

Fig. 2 Timescales of variability in the simulated and observed SRI. **a** Comparison between FFT spectra from observation (CRU TS 3.24.01: 1901–2005) and 95 historical runs from 28 CMIP5 models (1850/60–2005). *Bold contour lines* show the probability limits at $p = 0.05$ based on 1000 Monte Carlo simulations of the red noise background spectrum. White crosses indicate area where FFT power spectral density could have been influenced by the sampling period. **b** Centred Ratio of standard deviation (1-rSD), here expressed in percentage, between simulations and observation according to the three dominant time-scales of variability. *Bold contour lines* indicates CMIP5 models simulating significantly equal SRI variance than observations at $p = 0.05$ according to the Fisher's F -test. Summary of the mean biases per timescales is provided on the bottom left corner (*all model simulations: black; model simulation overestimating [underestimating] interannual variability: blue [red]*).

Fig. 3 Summary of observed summer (NDJF) SA rainfall variability and its teleconnection with global SSTs at three different timescales. **a** Spatial patterns of rainfall standard deviations in observations (CRU TS 3.24.01). **b** Observed spatial patterns of global SST standard deviations (ERSSTv.4). *Bold red contour lines* delineates area where observed interannual to IDV variance are significantly greater than the red noise background spectrum at $p = 0.05$ based on 1000 Monte Carlo simulations. **c** Observed global SST composite anomalies (ERSSTv.4) during enhanced SRI fluctuations (± 1 SD: wet years minus dry years) at the three different timescales. Statistical significance (*contours*) has been estimated by testing the difference in mean between SST anomalies during periods of rainfall variability greater and lower than 1 SD, through a modified t -test accounting for pseudoreplication in the series at $p = 0.05$. Displayed composite SST anomalies refer to wet conditions in SA, but are strictly opposite during dry conditions (cf. Fig. A1).

Fig. 4 Evaluation of model performance and their diversity in simulating SA rainfall variance at three different timescales. **a-c** Taylor diagram of summer (NDJF) rainfall variance spatial patterns of 95 historical runs from 28 CMIP5 models (*coloured dot referring to each individual model; cf. Table 1*) and from observations (CRU TS 3.24.01; *grey dot*) at the IDV to interannual timescales. The diagram is a function of the root mean square (RMS, *green dashed circles—x-axis*), the correlation coefficient (*black dashed lines—y-axis*) and the SD (*blue dashed compared to solid circles—x-axis*). Since the values are normalized the reference (observation values) has a SD of 1. **d** Cluster diversity as determined using AHC, and in assessing significance of each cluster using multiscale bootstrapping. Colours indicate different clusters, and non-significantly clustered simulations are in white. Simulated rainfall fields have been remapped on a regular $0.5^{\circ} \times 0.5^{\circ}$ resolution grid to be compared to observation.

Fig. 5 Summer-rainfall variance over SA at three different timescales in CMIP5 models. **a-c** Spatial patterns of rainfall standard deviations in six selected clusters from full CMIP5 multimodel ensemble at the interannual to IDV timescales. *Dark red to dark blue contours lines on the bottom panels* delineates areas where IDV to interannual variance are significantly different than in observations at $p = 0.05$ according to the Fisher's F -test. The selected six clusters are ranked according to their variance (var), here expressed as the percentage of simulations in each cluster. Spatial correlations (cor[obs.]) between simulated and observed patterns are displayed for information purpose. *Asterisks* indicate significant Pearson's correlations at $p = 0.05$ between the cluster and the observed pattern. Note that QDV and IDV standard deviations have been multiplied by 2 for illustrative purpose. Simulated rainfall fields have been remapped on a regular $0.5^{\circ} \times 0.5^{\circ}$ resolution grid to be compared to observation.

Fig. 6 Evaluation of model performance and their diversity in simulating NDJF SST variance and global SST composite anomalies at three different timescales. **a** Taylor diagram of NDJF SST variance spatial patterns of 95 historical runs from 28 CMIP5 models (*coloured dot referring to each individual model; cf. Table 1*) and from observations (ERSSTv.4; *grey dot*) at the IDV to interannual timescales. **b** as for **a** but for SST composite anomalies during enhanced SRI (± 1 SD: wet years minus dry years). **c** Cluster diversity for global SST variance and composite anomalies as determined using AHC, and in assessing significance of each cluster using multiscale bootstrapping. Colours indicate different clusters, and non-significantly clustered simulations are in white.

Fig. 7 NDJF global SST variance at three different timescales in CMIP5 models. **a-c** Spatial patterns of global SST standard deviations in six selected clusters from full CMIP5 multimodel ensemble at the interannual to IDV timescales. *Dark red to dark blue contours lines* delineates areas where SST variance are significantly different than in observations at $p = 0.05$ according to the Fisher's F -test. The selected six clusters are ranked according to their variance (var), here expressed as the percentage of simulations in each cluster. Spatial correlations (cor[obs.]) between simulated and observed patterns are displayed for information purpose. *Asterisks* indicate significant Pearson's correlations at $p = 0.05$ between clusters and the observed pattern.

Fig. 8 as **Fig. 7** but for global SST composite anomalies in the CMIP5 models. *Black and grey contours* indicate that statistical significance of composite anomalies was reached in 50% of the model defining the cluster. Composite anomalies and statistical significances have been estimated as defined in Figure 3. The selected six clusters are ranked according to their variance (var), here expressed as the percentage of simulations in each cluster. Spatial correlations (cor[obs.]) between simulated and observed patterns are displayed for information purpose. *Asterisks* indicate significant Pearson's correlations at $p = 0.05$ between clusters and the observed pattern.

Fig. 9 Comparison of performances in simulating SRI variability and associated SST teleconnections in the different ocean basins. Percentage of CMIP5 simulations associated with contrasted performances in SST variability and associated teleconnections has been quantified. +SST/+SRI refers to simulations with good SRI variability (*i.e.* significantly equal variance according to a Fisher F-test at $p = 0.05$) and good SST teleconnection patterns (*i.e.* Person correlations with observation ≥ 0.5). OppSST indicates simulations with good SRI variability, but opposite SST teleconnection patterns (*i.e.* Person correlation with observation < 0). +SST/-SRI refers to simulations with poor SRI variability (*i.e.* not significantly equal variance according to a Fisher F-test at $p = 0.05$), but with good SST teleconnection patterns. -SST/+SRI denotes simulations with good SRI variability, but with poor SST teleconnection patterns (*i.e.* Person correlations with observation < 0.5).

Fig. 10 Sample size uncertainties and model capabilities at the three different timescales. **a** Capability to simulate observed SRI variance (significant equal variance according to a Fisher F-test at $p = 0.05$) in all historical runs from the 28 CMIP5 models (*top*), and in their associated pi-Control runs (*bottom*). **b** Capability to simulate similar teleconnections (*i.e.* Pearson correlations ≥ 0.5) in all historical runs from the 28 CMIP5 models (*top*), and in their associated pi-Control runs (*bottom*). Grey dot sizes refer to the number of samples used to estimate the model capabilities, and should be used as an indicator of robustness.

Fig. 11 Atmospheric bridges between the Pacific Ocean and SA in 20CR.v2c. NDJF velocity potential (ϕ ; *shaded*) and stream function (ψ ; *contours*) composite anomalies between 850 and 600 hPa (*left*), and between 400 and 150 hPa (*right*), during enhanced SRI fluctuations (± 1 SD: wet years minus dry years) at the three different timescales. Composite anomalies and statistical significances have been estimated as defined in Figure 3. Only significant velocity potential and stream function anomalies at $p = 0.05$ are displayed. Note: IDV anomalies are multiplied by 1.5 to be clearly displayed.

Fig. 12 Atmospheric bridges between the Pacific Ocean and SA in selected CMIP5 models. **a-c** Simulated NDJF velocity potential (ϕ ; *shaded*) and stream function (ψ ; *contours*) composite anomalies between 850 and 600 hPa during enhanced SRI fluctuations (± 1 SD: wet years minus dry years) at the three different timescales. Composite anomalies and statistical significances have been estimated as defined in Figure 3. Only significant velocity potential and stream function anomalies at $p = 0.05$ are displayed. Note: IDV anomalies are multiplied by 1.5 to be clearly displayed.

Fig. A1 Comparison between SST composite anomalies associated with wet and dry conditions in SA. **a-c** Scatterplot of observed SST composite anomalies during wet (positive SRI anomalies = +1 SD) and dry (negative SRI anomalies = -1 SD) conditions at the interannual (left), QDV (middle) and IDV (right) timescales. **d-f** as **a-c** but for 95 historical runs from 28 CMIP5 models. Scatter plots are smoothed and coloured (*low to high probability = blue, yellow to red*) using a 2D kernel density estimate. Red and black lines refer to the regression lines between wet and dry SST composite anomalies, and associated correlation coefficients are provided in the lower left corner on each panel.

Fig. A2 Step-by-step process of the multi-scale bootstrap clustering. Step-0: 10 simulated patterns of global SST variability are submitted to the clustering approach. Step-1: simulated patterns are resampled n_i times, using r_j scales (referring to different sizes of the spatial domain). Step-2: $n_i \times r_j$ Agglomerative hierarchical clustering are produced, using Ward's agglomerative criteria applied to Euclidian distances. Step-3: the probability of each simulations to be clustered with the others (red values) is estimated. Here, only two clusters are significantly robust at $p \geq 0.90$.

Fig. A3 Percentage of occurrence of significant signals within the interannual, QDV and IDV timescales of SRI variability in all (95) model simulations, in all (28) models and all (16) institutions using the CMIP5 historical experiments. Statistical significance was estimated at $p=0.05$ based 1000 Monte Carlo simulations of the red noise background spectrum.

Fig. A4 Boxplots of the correlations between simulations of the same models (intra-ensembles; blue), and of different models (inter-models; red), of the CMIP5 historical experiments in reproducing spatial patterns of SA rainfall variability at the three different timescales.

1192

1193 **Fig. A5** Distributions of model simulations in clustering patterns of SA rainfall variability,
1194 global SST variability, and teleconnections at the interannual to interdecadal timescales. The
1195 six selected clusters, which are shown in Figures 5, 7 and 8, are in bold.

1196

1197 **Fig. A6** Boxplots of the correlations between simulations of the same models (intra-ensembles;
1198 blue), and of different models (inter-models; red), of the CMIP5 historical experiments in
1199 reproducing spatial patterns of global SST variability (shaded), and SST composite anomalies
1200 associated with SA rainfall variability (not shaded) at the three different timescales.

1201

1202 **Fig. A7** Mean annual cycle of monthly standard deviations of SST anomalies over the Niño3.4
1203 region (*i.e.* 5°S-5°N and 120-170°W) in the CMIP5 models (*coloured contours refer to each*
1204 *individual model; cf. Table 1*) and in the CRU TS 3.24.01 observations (*grey shaded*). SST
1205 anomalies are here calculated by subtracting the monthly climatology according to the
1206 definition of the Niño3.4 index (Trenberth 1997). To reduce the influence of the global trends,
1207 SST anomalies are detrended using a locally weighted linear regressions, with span equal to the
1208 length of the data.

Figure 1

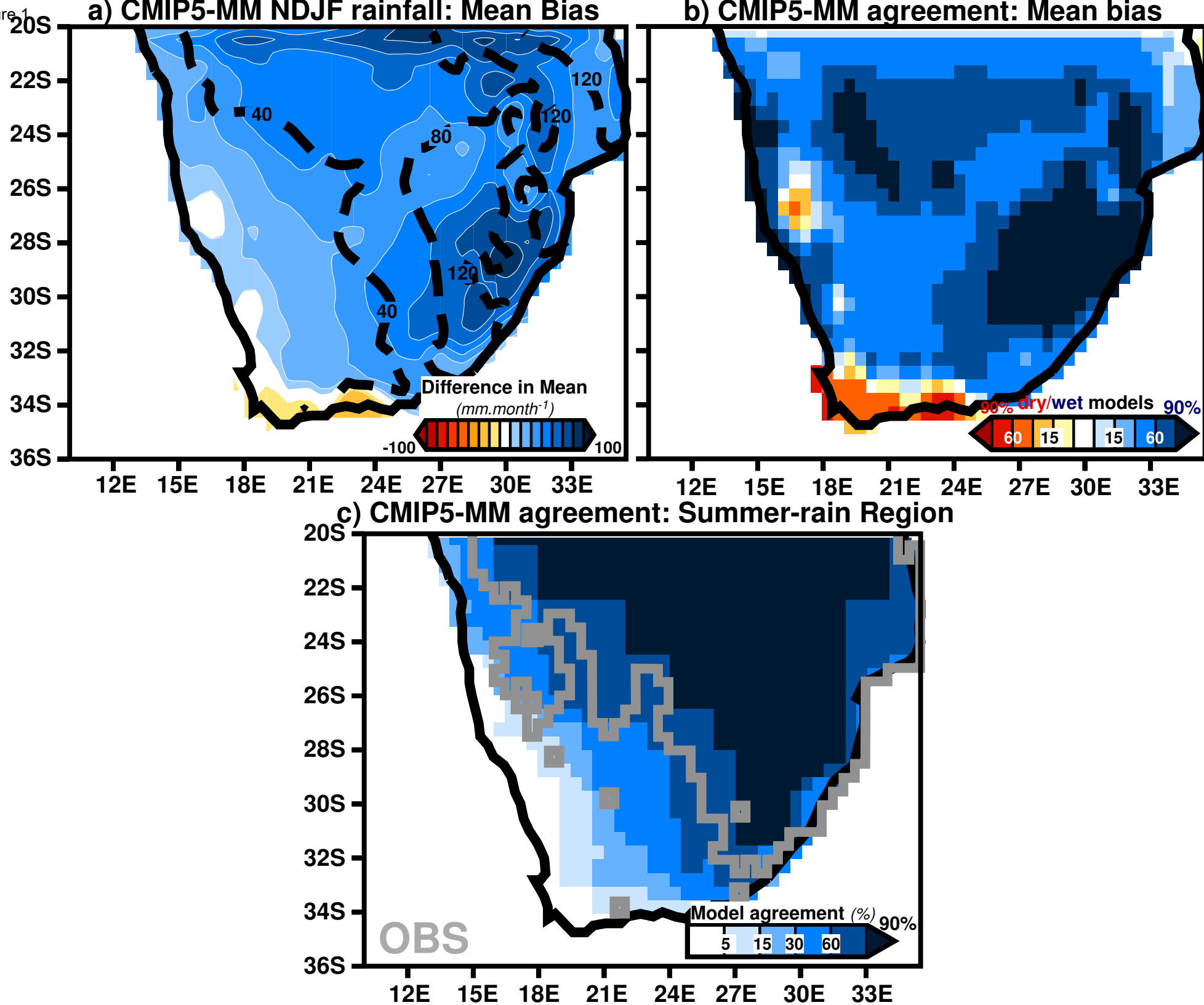


Figure 2

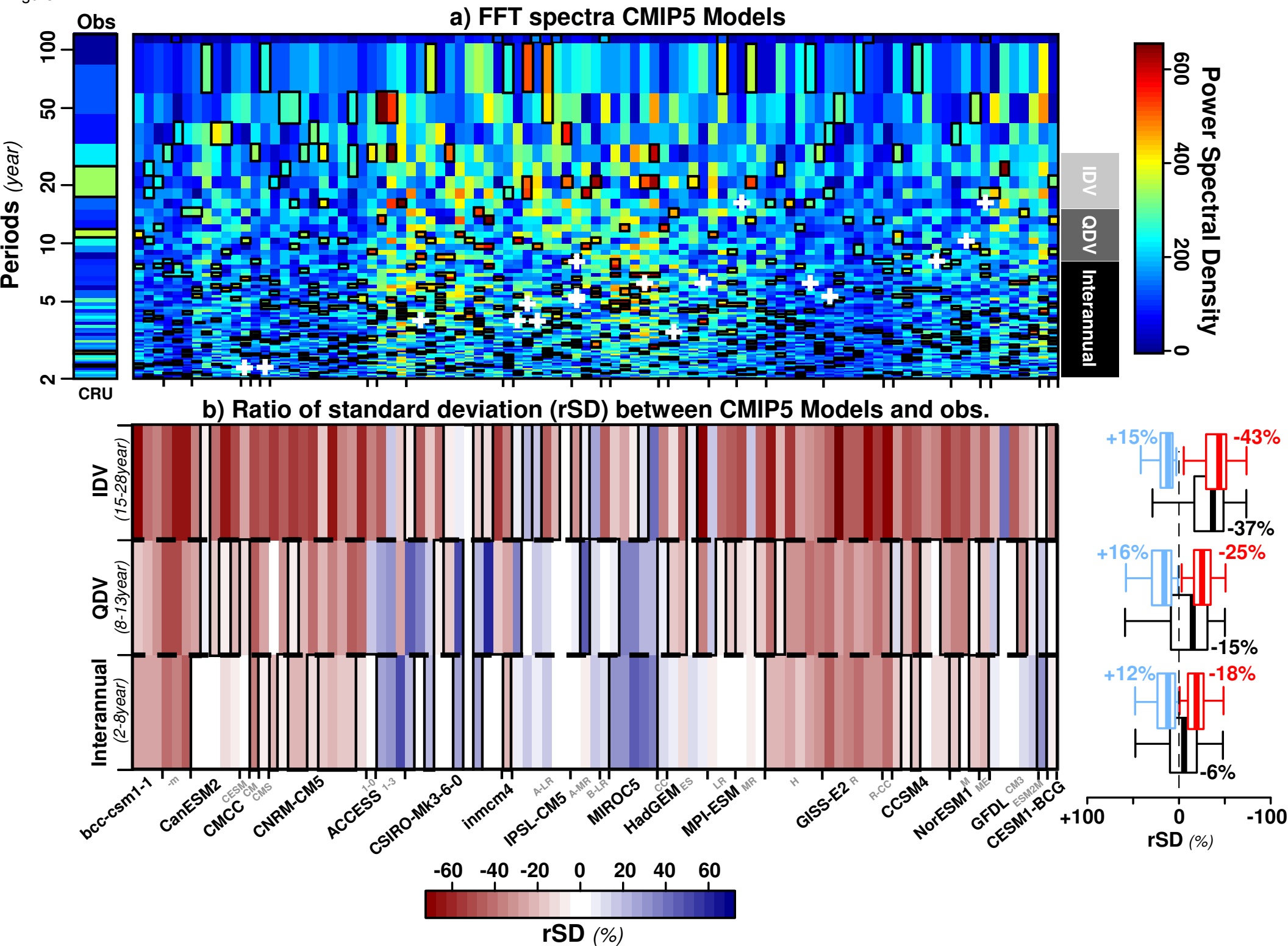


Figure 3

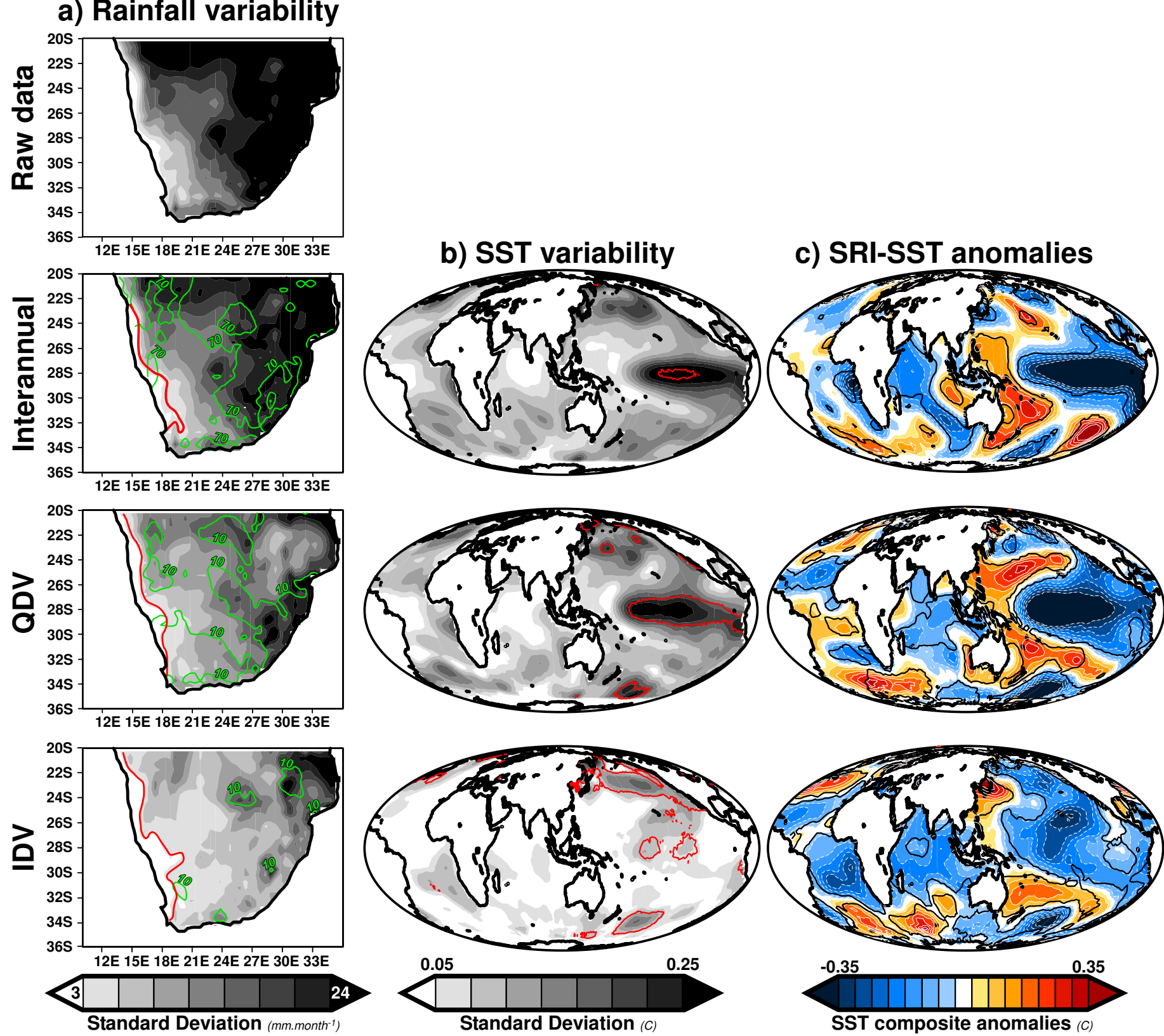


Figure 1

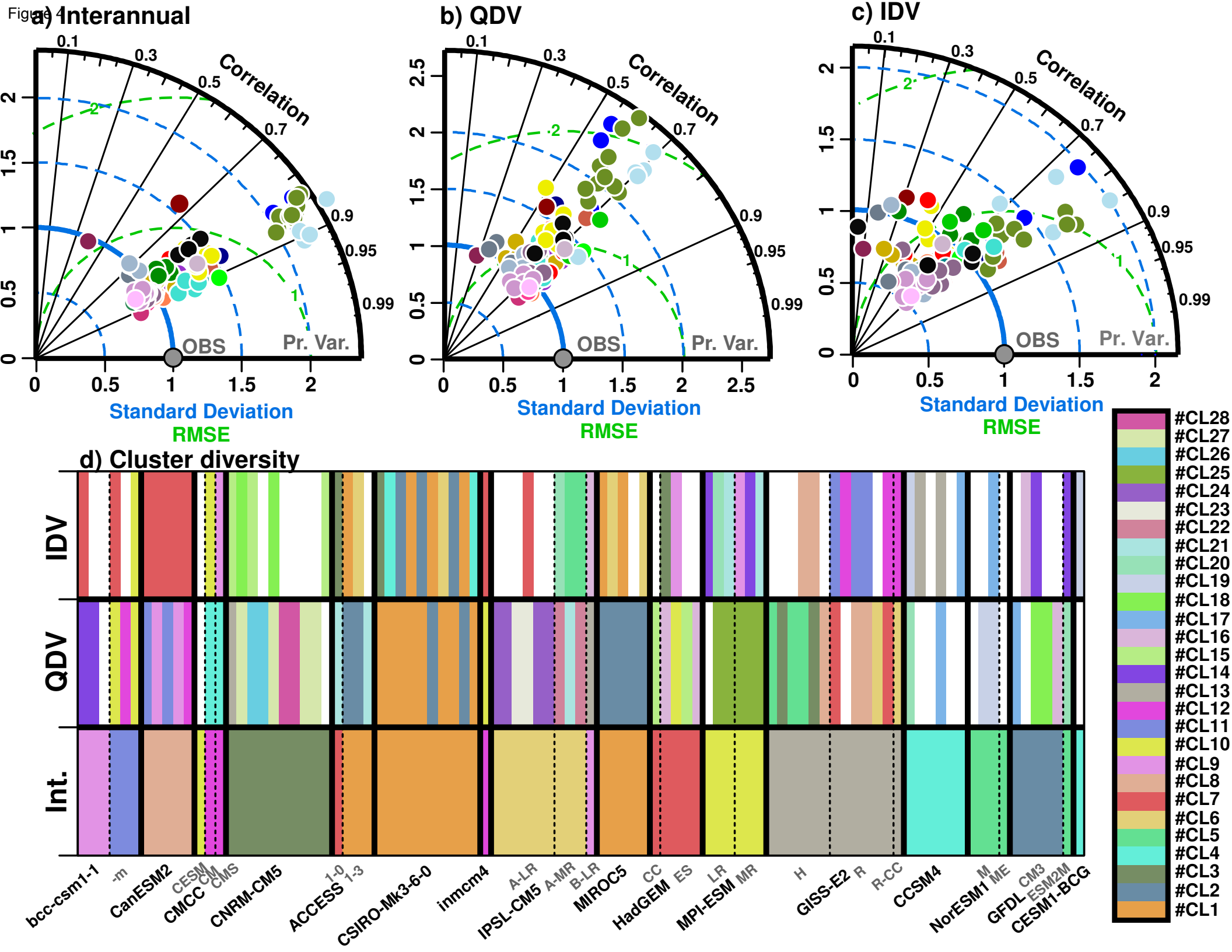


Figure 5

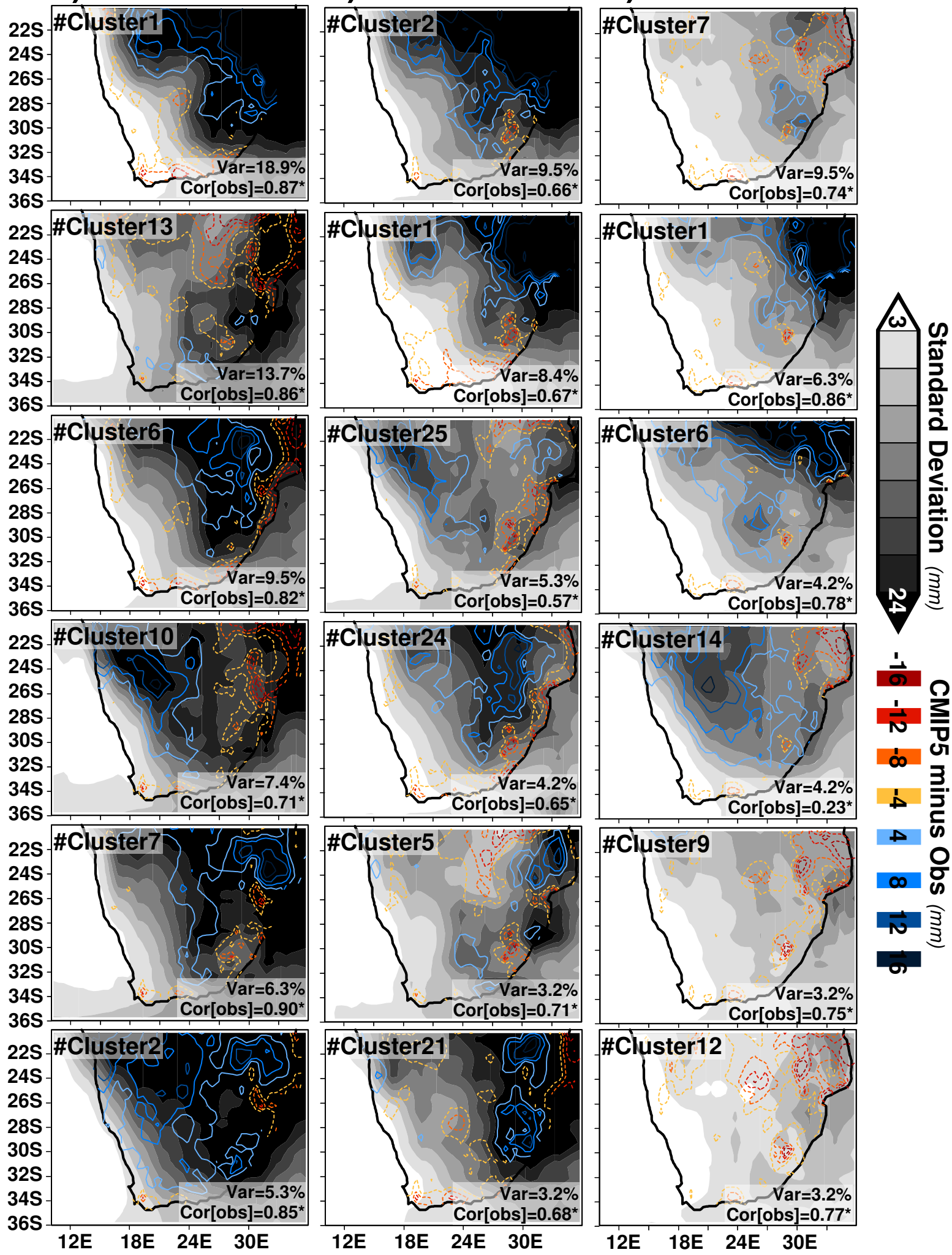
a) CMIP5 Int.**b) CMIP5 QDV****c) CMIP5 IDV**

Figure 6

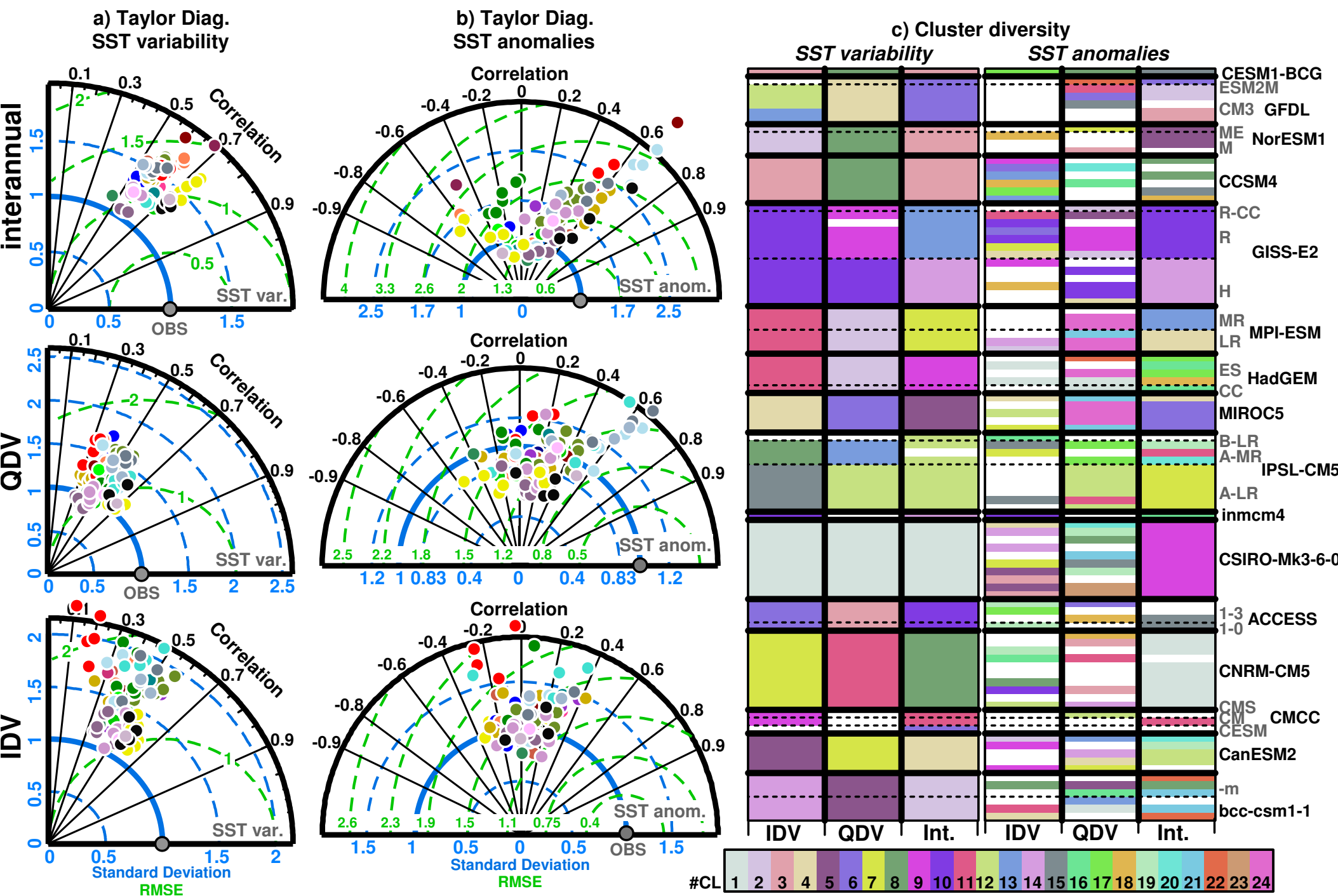


Figure 7

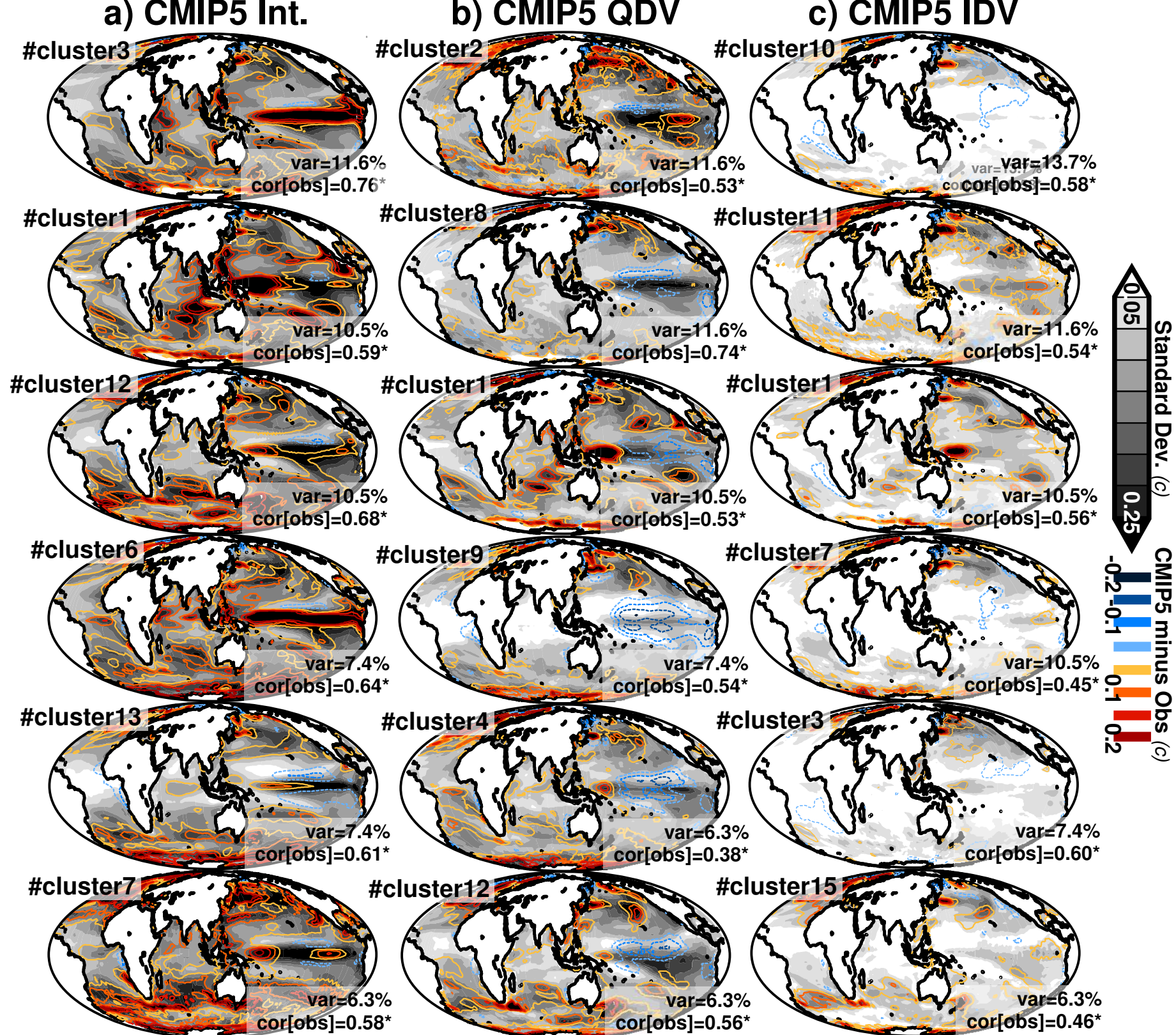


Figure 8

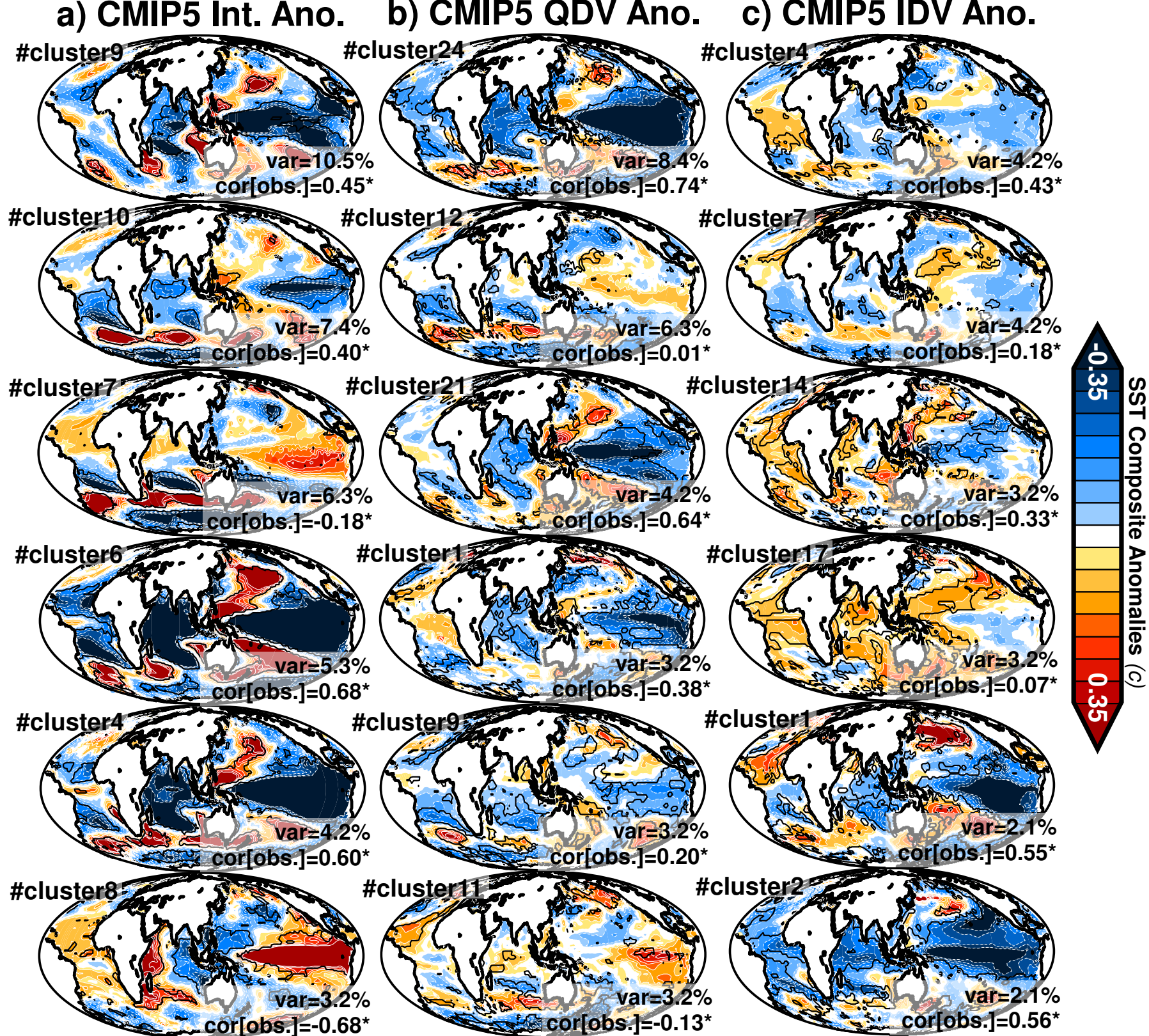


Figure 9

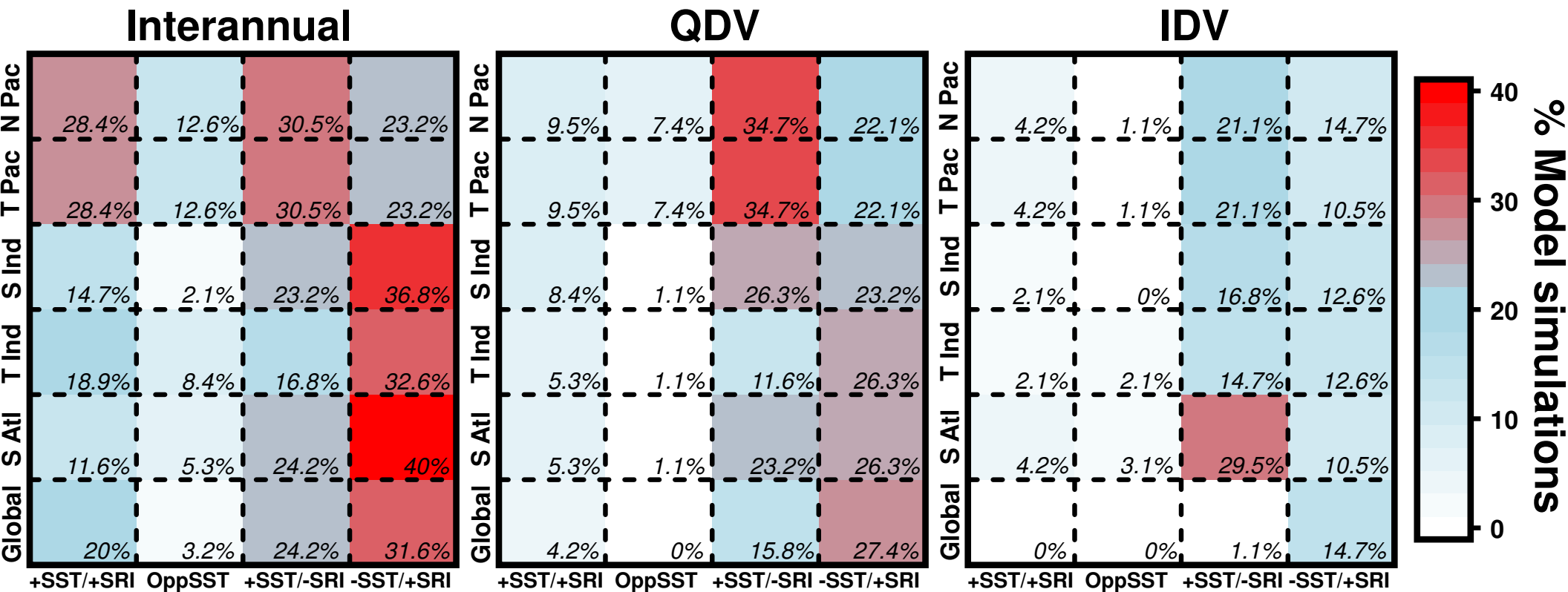


Figure 10

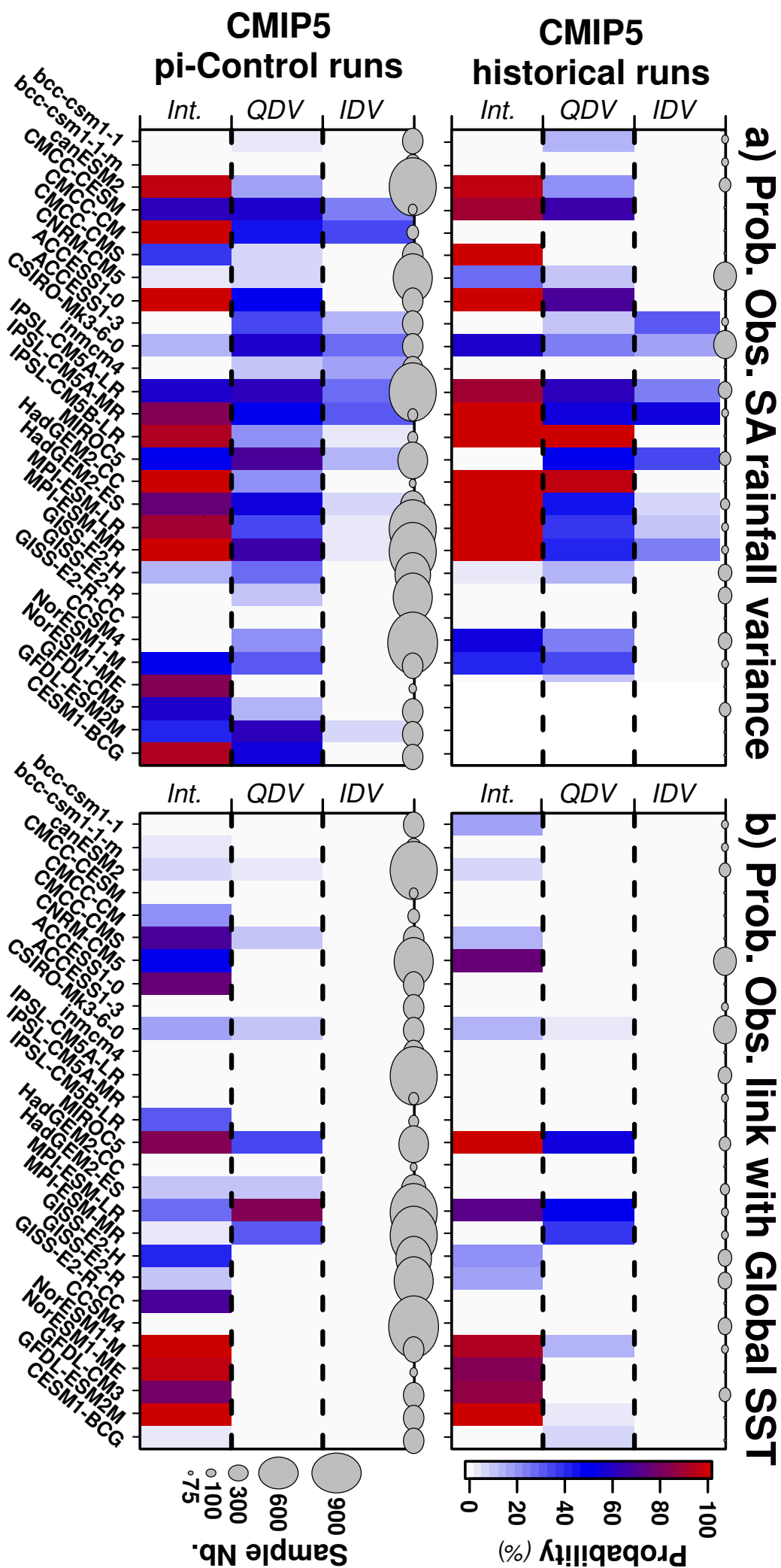


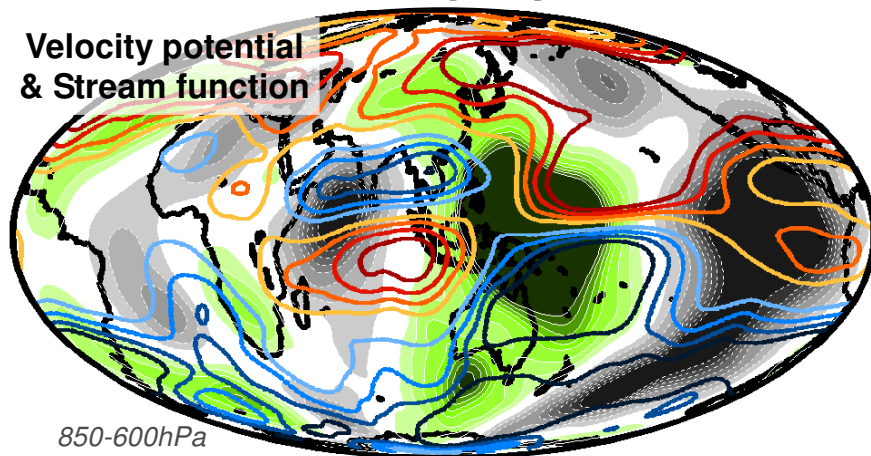
Figure 11

Lower Troposphere

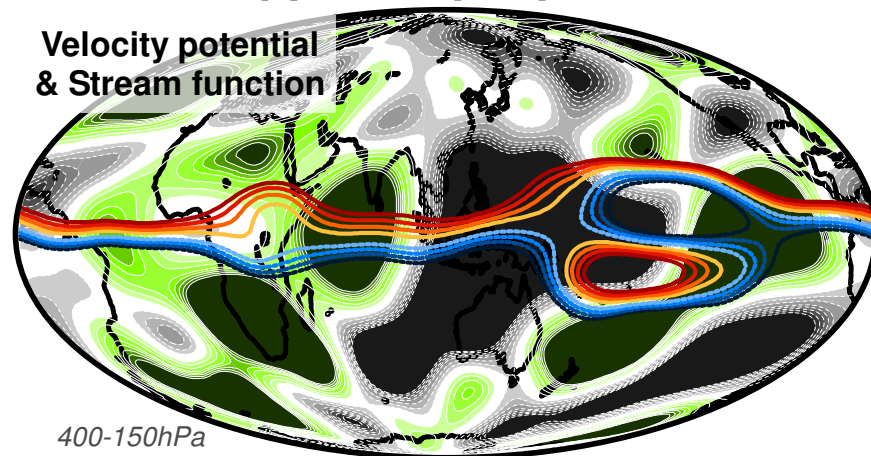
Upper Troposphere

Interannual

Velocity potential
& Stream function

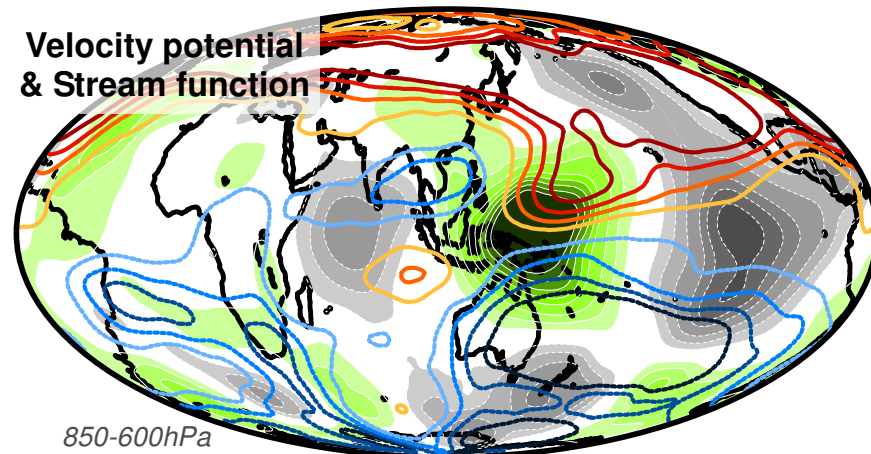


Velocity potential
& Stream function

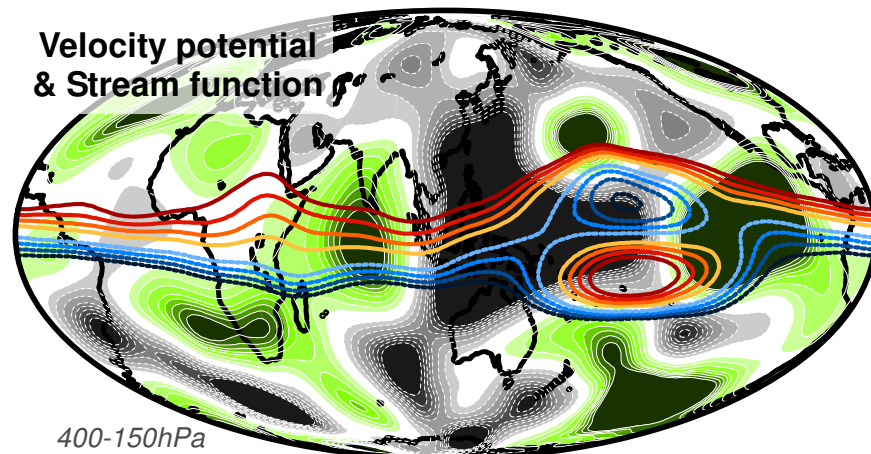


QDV

Velocity potential
& Stream function

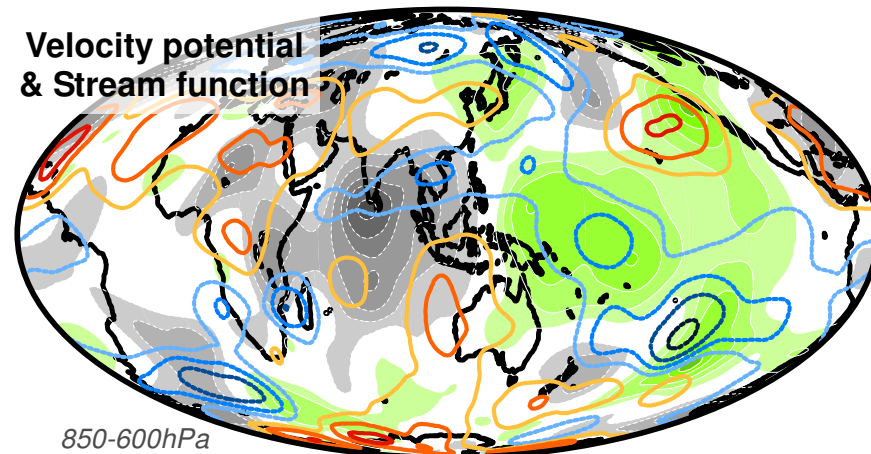


Velocity potential
& Stream function

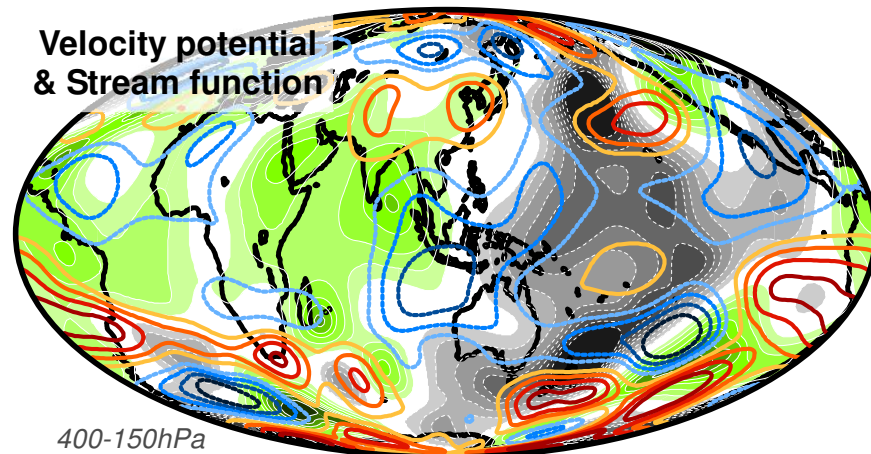


IDV

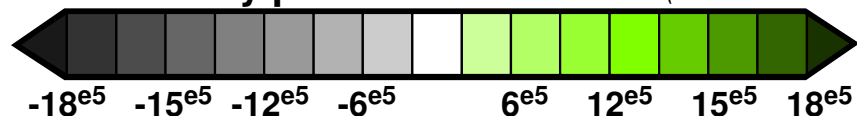
Velocity potential
& Stream function



Velocity potential
& Stream function



Velocity potential anomalies ($m^2.s^{-1}$)



Stream function anomalies ($m^2.s^{-1}$)



Figure 12

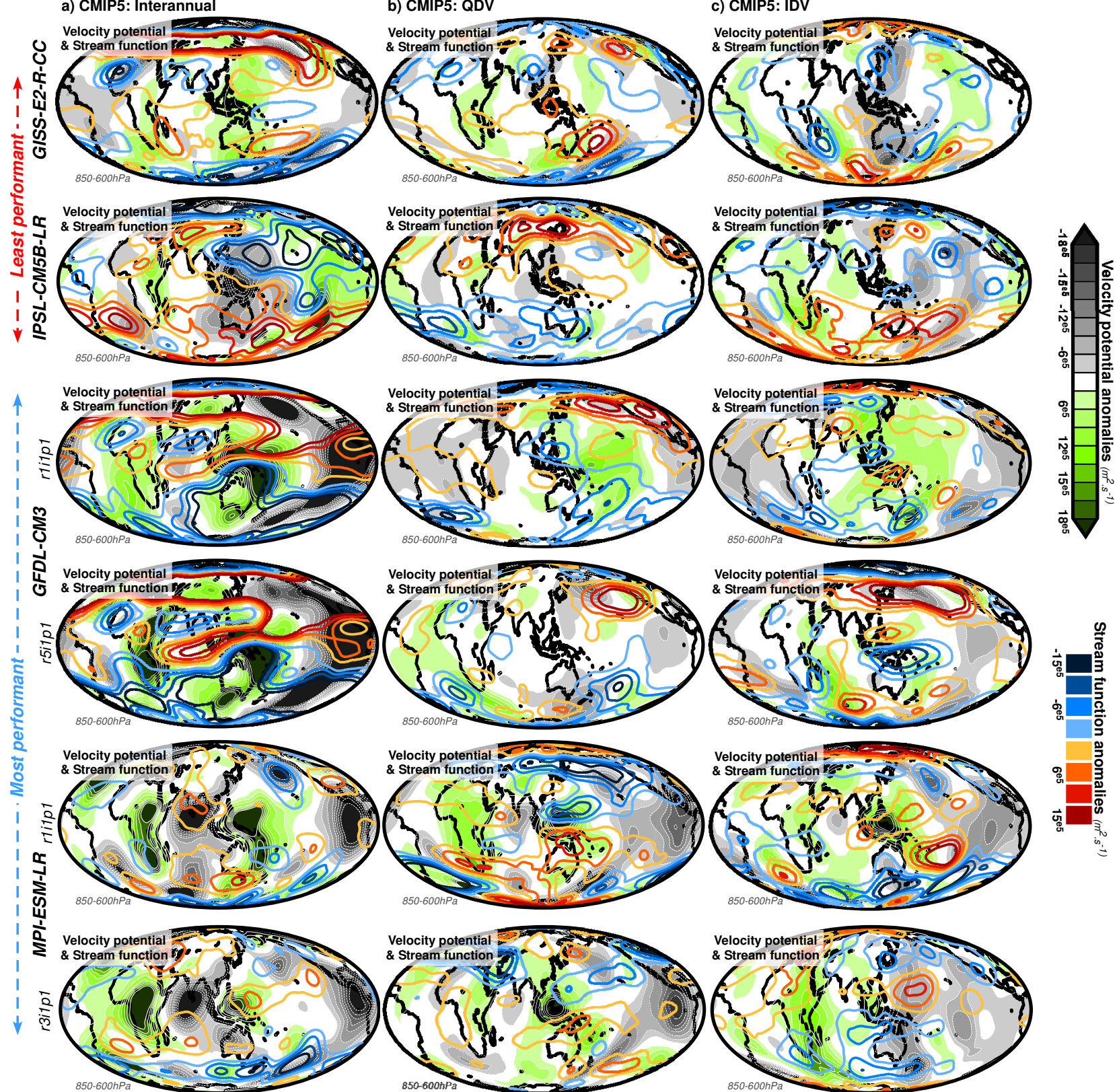


Table 1





























Obs.	CMIP5 Model outputs									
	CRU, UK	CRU TS 3.24.1	0	pr	1901-2014	0	1 x 1	0		
	NOAA-NCDC, USA	ERSS.v4	0	sst		0	0	0		
	NOAA-CIRES, USA	20CR.v2c	56	φ, ψ		0	2 x 2	0		
	BCC, China	bcc-csm1-1	3	pr, sst, φ, ψ	1850-2005	500	2.7906 x 2.8125			
		bcc-csm1-1-m	3			400	1.13 x 1.13			
	CCCma, Canada	CanESM2	5	pr, sst, φ, ψ	1850-2005	996	2.7906 x 2.8125			
	CMCC, Italy	CMCC-CESM	1			277	3.4431 x 3.75			
		CMCC-CM	1	pr, sst, φ, ψ	1850-2005	329	0.7484 x 0.75			
		CMCC-CMS	1			500	3.7111 x 3.75			
	CNRM, France	CNRM-CM5	10	pr, sst, φ, ψ	1850-2005	850	1.4008 x 1.40625			
	CSIRO-BOM, Australia	ACCESS1-0	1	pr, sst, φ, ψ	1850-2005	500	1.25 x 1.875			
		ACCESS1-3	3			500				
	CSIRO-QCCCE, Australia	CSIRO-Mk3-6-0	10	pr, sst, φ, ψ	1850-2005	500	1.8653 x 1.875			
	INM, Russia	inmcm4	1	pr, sst, φ, ψ	1850-2005	500	1.5 x 2			
		IPSL-CM5A-LR	6			1000	1.8947 x 3.75			
	IPSL, France	IPSL-CM5A-MR	3	pr, sst, φ, ψ	1850-2005	300	1.2676 x 2.5			
		IPSL-CM5B-LR	1			300	1.8947 x 3.75			
	MIROC, Japan	MIROC5	5	pr, sst, φ, ψ	1850-2005	670	1.4008 x 140625			
	MOHC, UK	HadGEM2-CC	1	pr, sst, φ, ψ	1860-2005	240	1.25 x 1.875			
		HadGEM2-ES	4			577				
	MPI-M, Germany	MPI-ESM-LR	3	pr, sst, φ, ψ	1850-2005	1000	1.8653 x 1.875			
		MPI-ESM-MR	3			1000				
	NASA-GISS, USA	GISS-E2-H	6			780				
GISS-E2-R		6	pr, sst, φ, ψ	1850-2005	850	2 x 2.5				
GISS-E2-R-CC		1			251					
NCAR, USA	CCSM4	6	pr, sst, φ, ψ	1850-2005	1051	1.25 x 0.94				
NCC, Norway	NorESM1-M	3	pr, sst, φ, ψ	1850-2005	501	1.8947 x 2.5				
	NorESM1-ME	1			252					
NOAA-GFDL, USA	GFDL-CM3	5	pr, sst, φ, ψ	1860-2005	500	2 x 2.5				
	GFDL-ESM2M	1		1861-2005	500	2.0225 x 2.5				
NSF-DOE-NCAR, USA	CESM1-BCG	1	pr, sst, φ, ψ	1850-2005	500	1.25 x 0.94				

Table 2

CMIP5 Model outputs						
Institution	Name	Atmospheric Comp.	Ocean Comp.	Land Comp.	Sea-Ice Comp.	
BCC, China	bcc-csm1-1-1	BCC-AGCM2-1	MOM4-1	BCC-AVIM1-0	SIS	
	bcc-csm1-1-m	BCC-AGCM2-1				
CCCma, Canada	CanESM2	CanCM4	CanOM4	CTEM	o	
CMCC, Italy	CMCC-CESM	ECHAM5	OPA8-2	SILVA	LIM	
	CMCC-CM					
	CMCC-CMS					
CNRM, France	CNRM-CM5	ARPEGE	NEMO3-2	ISBA	GELATO	
CSIRO-BOM, Australia	ACCESS1-0	HadCM3	MOM4-1	MOSES2	CICE	
	ACCESS1-3	MO GA1-0				
CSIRO-QCCCE, Australia	CSIRO-Mk3-6-0	CSIRO-Mk3	MOM2-2	o	~CICE	
INM, Russia	inmcm4	INMAM	INMOM	o	o	
IPSL, France	IPSL-CM5A-LR	LMDZ5A	NEMO3-2	ORCHIDEE	LIM	
	IPSL-CM5A-MR					
	IPSL-CM5B-LR	LMDZ5B				
MIROC, Japan	MIROC5	FRCGCM	COCO	MATSIRO	COCO	
MOHC, UK	HadGEM2-CC	HadCM3	HadGOM1	MOSES2	CICE	
	HadGEM2-ES					
MPI-M, Germany	MPI-ESM-LR	ECHAM6	MPI-OM	JSBACH	o	
	MPI-ESM-MR					
NASA-GISS, USA	GISS-E2-H	ModelE2	Russel	o	o	
	GISS-E2-R					
	GISS-E2-R-CC					
NCAR, USA	CCSM4	CAM4	POP	CLM4	CICE	
NCC, Norway	NorESM1-M	CAM4	MICOM	CLM4	CICE	
	NorESM1-ME					
NOAA-GFDL, USA	GFDL-CM3	AM3 AM2	MOM4-1	LM3	SIS	
	GFDL-ESM2M					
NSF-DOE-NCAR, USA	CESM1-BCG	CAM4	POP2	CLM4	CICE	